

Characterization of uncertainties in electron-argon collision cross sections under statistical principles

Seung Whan Chung¹, Todd A. Oliver¹, Laxminarayan L. Raja²,
Robert D. Moser^{1,3}

¹ Oden Institute for Computational Engineering and Sciences, University of Texas at Austin, 201 E. 24th Street, Austin, TX 78712

² Department of Aerospace Engineering & Engineering Mechanics, University of Texas at Austin, 2617 Wichita Street, Austin, TX 78712

³ Walker Department of Mechanical Engineering, University of Texas at Austin, 204 E. Dean Keeton Street, Austin, TX 78712

E-mail: chung28@llnl.gov

June 2023

Abstract. The predictive capability of a plasma discharge model depends on accurate representations of electron-impact collision cross sections, which determine the key reaction rates and transport properties of the plasma. Although many cross sections have been identified through experiments and quantum mechanical simulations, their uncertainties are not well-investigated. We characterize the uncertainties in electron-argon collision cross sections using a Bayesian framework. Six collision processes—elastic momentum transfer, ionization, and four excitations—are characterized with semi-empirical models, whose parametric uncertainties effectively capture the features important to the macroscopic properties of the plasma, namely transport properties and chemical reaction rates. The method is designed to capture the effects of systematic errors that lead to large discrepancies between some data sets. Specifically, for the purposes of Bayesian inference, each of the parametric cross section models is augmented with a Gaussian process representing systematic measurement errors as well as model inadequacies in the parametric form. The results show that the method is able to capture scatter in the data between the electron-beam experiments and *ab-initio* quantum simulations. The calibrated cross section models are further validated against measurements from swarm-parameter experiments.

Submitted to: *arXiv preprint*

1. Introduction

Determining cross sections for atomic and molecular collision processes is crucial to the accuracy of plasma discharge model predictions [1]. Most macroscopic observables of plasma, such as pressure or temperature, are features of the energy distribution functions of the particles that comprise the plasma [2]. The evolution of these energy

distribution functions is governed by the species Boltzmann equation, in which the cross sections appear in the collision term that represents the effects of particle interactions. Chemical reactions and transport processes are the macroscopic averages of these collision processes [3–5], and thus are determined by both the cross sections themselves and the energy distributions. In this context, electron-impact collisions are particularly important for modeling non-equilibrium plasmas [6, 7], where the energy distribution functions cannot be determined from equilibrium considerations.

Because of these dependencies, particle collision cross sections are necessary for a plasma discharge model. They are clearly essential for simulations based on the Boltzmann equations, where they appear explicitly. In particle-based Monte-Carlo simulations of the Boltzmann equation, these cross sections are used to statistically determine the collision rates [8–12]. In grid-based Boltzmann equation simulations, on the other hand, the collision rates are evaluated deterministically as expectations over the evolving distributions [13–15]. In either case, the cross sections—represented as functions of electron energy, either by an analytical model or a tabulated data—are direct inputs to the model. Further, even in fluid-based models where the cross sections do not appear explicitly in the model PDEs, the input data—specifically, reaction rates and transport properties—are dependent on the underlying cross sections [16]. Because of this importance, the characterization of collision cross sections has been a focus of experimental measurements for many decades and, more recently, *ab initio* quantum mechanics simulations. This work has resulted in numerous databases of cross sections, e.g., [17–21].

Unfortunately, the determination of collision cross sections is subject to uncertainties. These uncertainties arise from experimental or numerical errors in measuring the cross sections, and from uncharacterized systematic errors intrinsic to these studies [1]. Because of the importance of the cross sections to the characteristics of a plasma, their uncertainty results in uncertainties in the predicted plasma properties when the cross sections are used in a plasma simulation. To quantify uncertainties in the predictions, it is necessary to quantify the uncertainties in the cross sections. Such uncertainty quantification (UQ) allows the reliability of simulation predictions to be assessed and provides a basis for interpreting discrepancies between simulations and experiments [22, 23]. A representation of collision cross sections for use in a plasma simulation should therefore include uncertainties. Here we propose an uncertain cross section formulation which is informed by data from multiple sources using Bayesian inference [24–26]. To illustrate the cross section uncertainty quantification process, we consider six important electron collision processes with the ground-state argon atom. The collision processes are elastic momentum-transfer, direct ionization, and direct excitation to the four $1s$ excited states. The same UQ process can be similarly applied to any other collision process, assuming the necessary data are available.

There have been many studies to measure electron-impact cross sections in argon. They are generally of three types: electron beam experiments, swarm experiments and *ab initio* quantum calculations. These experiments and their uncertainties are discussed

briefly below. Detailed reviews of cross section measurements are available in [1, 6, 7, 27].

Electron-beam experiments measure the scattering of a mono-energetic electron beam, to determine differential cross sections at specific energies and angles [1, 27]. Combined with optical techniques, they can also measure excitation cross sections [28–30]. These are direct measurements of the cross sections, which are generally reported with an assessment of the experimental uncertainties. However, the measurements also involve systematic errors that are difficult to assess and vary from experiment to experiment [1]. As a result there are discrepancies among datasets from electron-beam experiments that are large compared to their reported uncertainties.

Electron swarm experiments measure electron transport parameters in swarms of electrons, which depend on the collision cross sections [1, 6, 27]. Obtaining the cross sections from the transport properties determined in the swarm experiments requires an inference procedure involving the (usually simplified) Boltzmann equation, in which many collision processes are active simultaneously [31–35]. In this analysis, it is often necessary to employ prior information on cross sections from other sources, either for a certain energy range or for a particular collision process [6]. Uncertainties in the inferred cross sections arise from the error in measuring the electron transport properties, errors arising from the simplifications in the analysis and from the uncertainties in the cross sections from other sources that are adopted in the analysis. The latter two uncertainties generally go uncharacterized.

Aside from experiments, *ab initio* quantum calculations also provide cross section data [6, 7]. These calculations involve the wavefunctions of a colliding electron and atom solved through approximate forms of Schrödinger’s equation. The cross section is computed as a dependent variable [36–38]. Among various *ab initio* datasets, the BSR data provides a comprehensive set of electron-argon collision cross sections [36, 39–42]. The resulting cross section data for noble gases agree well with experimental data. While the errors arising from the approximate model remain uncharacterized, the data is considered credible based on its accurate prediction and its low dependency on other (uncertain) sources.

Most reviews of cross section datasets from different sources [1, 6, 7] compare them and report their discrepancies. These discrepancies can be interpreted as arising from the unquantified uncertainties associated with the various datasets as described above. However, naively taking these discrepancies as a direct measure of uncertainty would be problematic for two reasons. First, such a characterization would not represent the correlation of errors at different collision energies. Second, in swarm analysis the datasets are often inter-dependent because they share sources of externally provided cross section data [6]. As a result, the discrepancy among swarm datasets understates the uncertainties.

In this paper, we develop an uncertain representation of electron-argon neutral collision cross sections as a function of collision energy. The approach accounts for both the estimated uncertainty in the available data and the systematic errors exposed by the inconsistency between datasets. The representation is based on semi-empirical

cross section models which include a few tunable parameters [1, 32, 43, 44], with an expectation that these parametric representations will be sufficient to capture the features of the cross sections that are essential to reaction rates and transport parameters in collisional plasma simulations. For other applications where one is interested in the cross section at specific energies, rather than integrated quantities, a richer representation may be necessary. The model parameters are considered uncertain, but to account for any errors introduced by the semi-empirical model form and the discrepancies introduced by unquantified systematic errors as discussed above, a Gaussian process representation of the error is also included [24]. A Gaussian process model is non-parametric, probabilistic representation of a function that is characterized by a number of hyperparameters. In the present work, Gaussian processes provide a flexible way to account for errors about which we do not have sufficient information to pose a parametric model.

For each collision, the semi-empirical model parameters and the Gaussian process hyperparameters are determined, with uncertainties, using Bayesian inference from the experimental and *ab initio* computational data described above. Because the aforementioned errors in the cross sections derived from swarm experiments are confounding and difficult to characterize, these results are not used for the Bayesian inference. Instead, the swarm data are reserved for validation of the probabilistic cross section model. Details of the data used for model calibration and validation are provided in Section 2.

In the remainder of the paper, the data are described in some detail (Section 2) and then the semi-empirical cross section models are introduced (Section 3). The Bayesian calibration formulation is described in Section 4, and the results of the Bayesian calibration and validation for three different formulations of the probabilistic error model are presented in Section 5. Finally, concluding remarks are provided in Section 6.

2. Cross section measurement datasets

The available data are split into two subsets: one consisting of electron-beam experiments and *ab initio* simulation results, which is used for calibration, and a second consisting of swarm experiment measurements, which is used for validation. The specific data sources as well as relevant features of the data are described for each of these subsets in Sections 2.1 and 2.2.

2.1. Electron-beam experiments and *ab initio* calculations

2.1.1. Data characterization The cross section data are curated from electron-beam experiments which at least notionally report their measurement accuracy [1, 6]. Table 1 and Figure 1 summarize the curated cross section data. Almost all experimental data are limited to energy $> 1\text{eV}$, and very low-energy data is scarcely available. The *ab-initio* calculation (BSR) by Zatsarinny and Bartschat [6, 18, 36] is also included in this study,

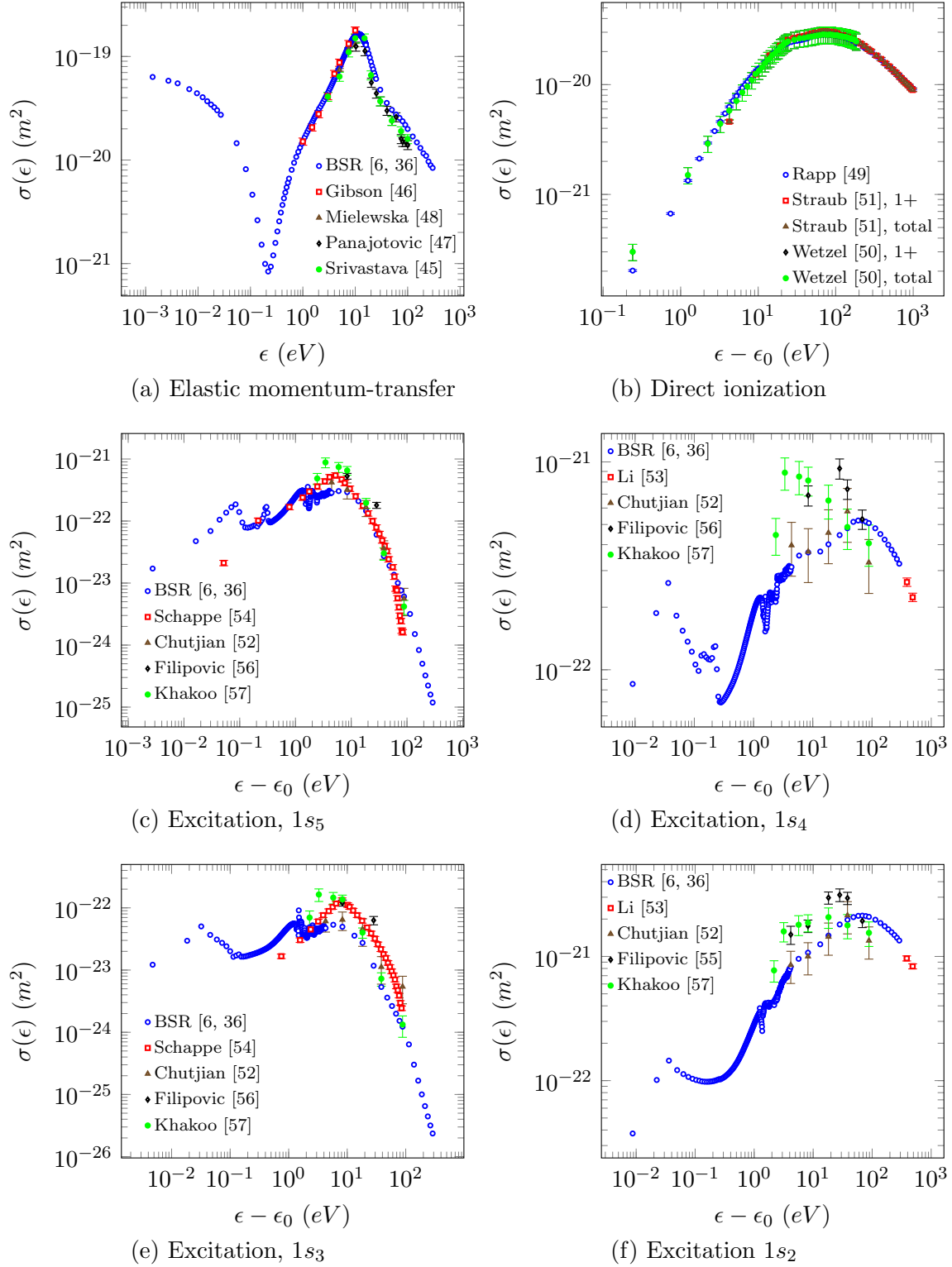


Figure 1. Electron-impact argon cross section data from the curated electron-beam experiments and *ab initio* calculation. The reported standard-deviation error, if available from the reference, is indicated as an error bar.

| Collision process | Author | Energy range ϵ (eV) |
|--|--|------------------------------|
| Elastic momentum-transfer, $\sigma_{el}(\epsilon)$ | Zatsarinny & Bartschat (BSR), 2013 [6, 36] | 10^{-3} –300 |
| | Srivastava <i>et al.</i> , 1981 [45] | 3–100 |
| | Gibson <i>et al.</i> , 1996 [46] | 1–10 |
| | Panajotovic <i>et al.</i> , 1997 [47] | 10–100 |
| | Mielewska <i>et al.</i> , 2004 [48] | 5–10 |
| Direct ionization (Ar^+), $\sigma_{ion}(\epsilon)$ | Rapp & Englander-Golden, 1965 [49] | Threshold– 10^3 |
| | Wetzel <i>et al.</i> , 1987 [50] | Threshold–200 |
| | Straub <i>et al.</i> , 1995 [51] | Threshold– 10^3 |
| Direct excitation, $\sigma_{ex}(\epsilon)$ | Zatsarinny & Bartschat (BSR), 2013 [6, 36] | Threshold–300 |
| | Chutjian & Cartwright, 1981 [52] ($1s_5$ – $1s_2$) | Threshold–100 |
| | Li <i>et al.</i> [53] ($1s_4$, $1s_2$) | 400, 500 |
| | Schappe <i>et al.</i> [54] ($1s_5$, $1s_3$) | Threshold–100 |
| | Filipovic <i>et al.</i> [55] ($1s_2$) | 16–80 |
| | Filipovic <i>et al.</i> [56] ($1s_5$ – $1s_3$) | 20–80 |
| | Khakoo <i>et al.</i> [57] ($1s_5$ – $1s_2$) | 14–100 |

Table 1. Summary of the curated electron-beam experiments and *ab initio* calculation.

which provides highly resolved data over a wide energy range. Though its accuracy is not reported, the data is considered credible based on its accurate prediction of atomic differential cross section from first-principles computation [36, 41, 42].

2.1.2. Discrepancies between datasets An observation from Figure 1 is the large discrepancies among datasets. Particularly for direct excitations in the 1 – 100 eV range, the datasets are scattered far outside the confidence intervals of each other, indicating that their reported measurement errors cannot fully explain the discrepancy.

This discrepancy is likely due to systematic errors that vary from experiment to experiment [1]. There can be several factors contributing to such errors. First, the detailed design of the electron gun varies between experiments as the energy range of interest usually spans from a few eV to several thousands of eV [1]. Also, the cross-beam technique, which is widely used for this type of experiment, is usually limited to relative measurements of the cross section, so the measurement is scaled with a reference value. The choice of this reference value can differ by experiments. For the elastic collision, the widely-used relative flow techniques often use the cross section of helium [45, 46, 48], or the same cross section from other measurements [47]; reflecting this point, Zatsarinny and Bartschat [39] also rescaled the experimental data from Buckman *et al.* [58] to compare with BSR dataset. Similarly for ionization, the measurement is sometimes normalized with respect to the cross section of hydrogen [49]; or the absolute value is measured at only one energy, and the measurements at other energy points are respectively scaled [51]. Likewise, the excitation cross sections are also normalized with previous measurements [52, 55–57]. Furthermore, many of these measurements

| Databases | Adopted (adjusted) cross sections | Reference |
|-------------------------------|--|--|
| Biagi/Biagi v7.1 [17, 34, 59] | σ_{el} ($< 1eV$) σ_{ex} σ_{ion} | Haddad & O'Malley [32] BSR [18, 36] Rapp & Englander-Golden [49], [51] |
| Hayashi [19, 60] | Compilation of 1960 literatures | |
| IST-Lisbon [20, 61] | σ_{el} σ_{ex} σ_{ion} | Phelps [62] Hayashi [60], [30, 43, 57, 63–66] Rapp & Englander-Golden [49] |
| Morgan [67] | not specified. | Phelps and Hayashi* [7] |
| Puech [21, 68] | σ_{el} ($0.014 \leq \epsilon \leq 4eV$) σ_{el} (otherwise) $\sigma_{ex}, \sigma_{ion}$ | Milloy <i>et al.</i> [31] Phelps [69] [43] |
| Phelps [69–71] | σ_{el} ($\epsilon < 4eV$) σ_{el} ($\epsilon > 8eV$) $\sigma_{ex,total}$ σ_{ion} | Milloy <i>et al.</i> [31] [72] [73] [74] |
| Nakamura [75] | σ_{el} ($\epsilon \leq 2.5eV$) σ_{el} ($\epsilon \geq 15eV$) $\sigma_{ex,total}$ σ_{ion} | Milloy <i>et al.</i> [31] [76] [77] Rapp & Englander-Golden [49] |
| Haddad (1982) [32] | σ_{el} ($\epsilon > 1eV$) | Milloy <i>et al.</i> [31] |

Table 2. References of adopted cross sections in swarm-analysis datasets from LXCat community. Authors of frequently adopted datasets are explicitly specified.

are obtained by integrating the corresponding differential cross section over angle using a numerical quadrature, where low-angle values are either extrapolated/adopted from other datasets [45, 47, 48, 52, 53, 55–57]. While Gibson *et al.* [46] utilized a phase-shift analysis to infer from the differential cross section, this involves a model-fitting procedure which likewise induces another systematic error. The optical emission measurements also involve multiple excitation and cascade processes, so measuring one of them requires approximation/estimation of the others [54].

There is not sufficient prior knowledge available to separate and independently quantify all these factors. However, simply neglecting this discrepancy leads to a significantly misleading conclusion for the uncertainty in the cross sections. Instead, a probabilistic model is introduced to account for the uncertainty implied by these discrepancies. The details of this model and its implications are discussed further in Section 4.

2.2. Swarm-analysis data

| Type | Reference | Swarm parameters | Condition |
|------------|---------------------------|---------------------------|----------------------|
| Transport | Townsend & Bailey [6, 78] | D_T/μ | |
| | Pack & Phelps [79] | $W = \mu E$ | 77K, 300K |
| | Warren & Parker [80] | D_T/μ | 77K, 88K |
| | Robertson & Rees [81] | D_L/μ | 90K, 700Torr/800Torr |
| | Robertson [82] | W | 89.6K, 293K |
| | Milloy & Crompton [83] | D_T/μ | 294K |
| | Kucukarpaci & Lucas [84] | $W, D_L\mu$ | 300K |
| | Al-Amin & Lucas [85] | D_T/μ | |
| | Nakamura & Kurachi [75] | $W, D_L/N$ | 300K |
| Ionization | Golden & Fisher [86] | α_{ion} | |
| | Kruithof [87] | | 273.15K |
| | Specht <i>et al.</i> [88] | | 300K |
| Excitation | Tachibana [29] | $\alpha_{ex} (1s_5-1s_2)$ | |
| | Biagi [17, 34, 59] | | 300K |
| | BSR [6, 18, 36] | | |
| | Hayashi [19, 60] | | |
| | IST-Lisbon [20, 61] | | |
| | Puech [21, 68] | | |

Table 3. Summary of swarm parameter experiment data.

2.2.1. Data chracterization Another type of widely used cross section data is based on swarm-analysis [1, 6]. The cross sections in these datasets are determined by requiring the transport properties and reaction rates as computed by using the cross sections in a zero-dimensional, two-term/multi-term Boltzmann solver to match those measured in the swarm parameter experiments. Some widely used cross section datasets from swarm analysis are listed in Table 2, and Table 3 summarizes the swarm parameter measurements used in this work. Further, these data are shown in Figure 2 and Figure 3.

The figures show that, the scatter among datasets for the same conditions is small compared to that of the electron-beam experiments. While the ionization Townsend coefficient from Specht *et al.* [88] deviates from other experiments at low energy, the authors recognized that in this regime their measurements include contributions from photoelectric emission by the metastables.

The experimental data for the direct excitation rate coefficients is scarce, since it is difficult to isolate these collision processes from others, especially radiative de-excitations. While we use the experimental data from Tachibana [29] who estimated these radiative de-excitation rates from the emission spectroscopy, we also adopt the swarm-analysis data from the LXCat community [6, 17–21], as shown in Figure 3. The excitation rate coefficients are obtained using a zero-dimensional Boltzmann solver (BOLSIG+ [16]), with the nominal cross section datasets [17–21]. The direct excitation rates to $2p$ -levels are also computed from the same datasets, which are then assumed

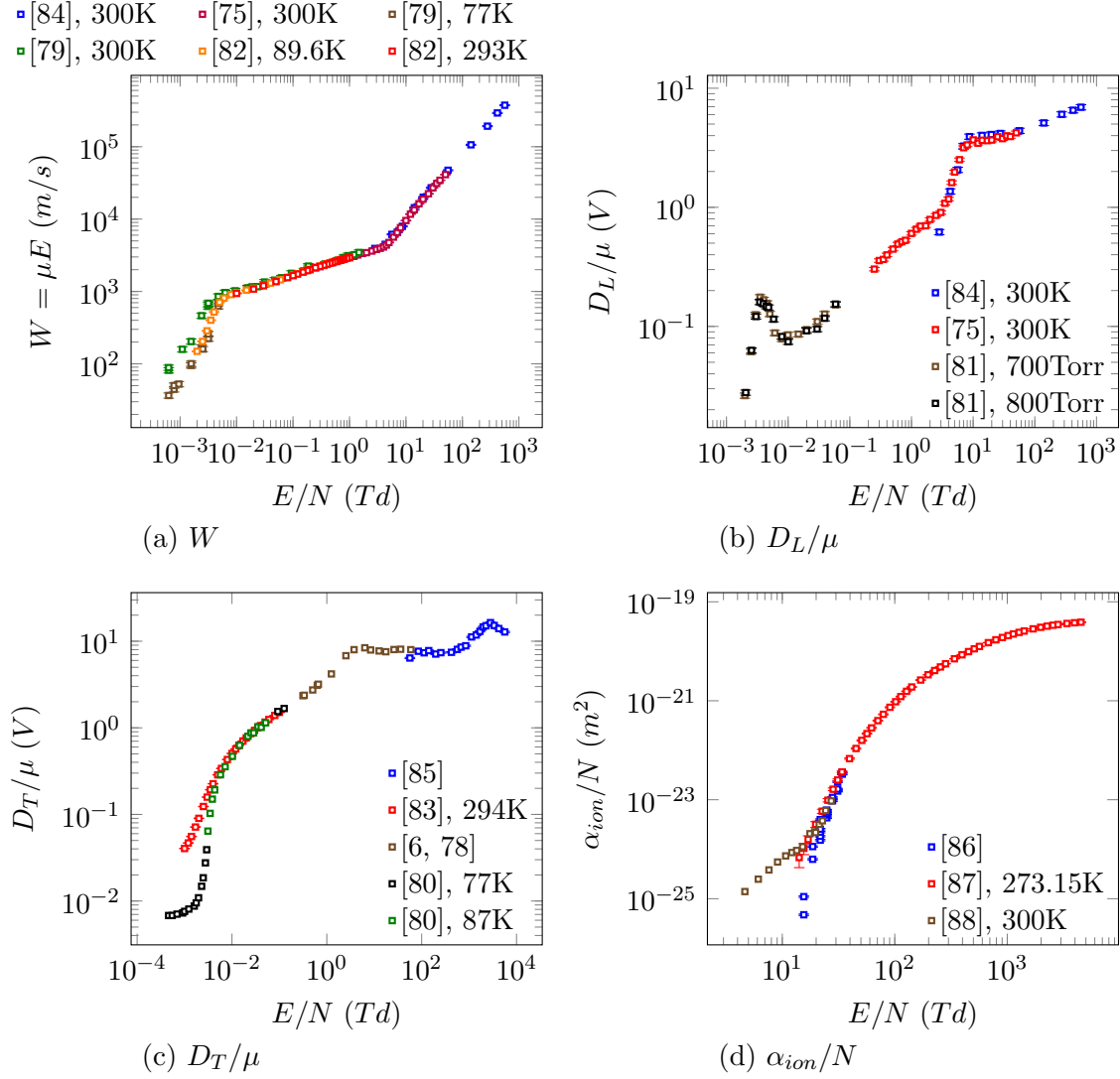


Figure 2. Swarm parameter experiment data used for validation of the calibrated cross sections: (a) drift velocity, (b) the ratio of longitudinal diffusivity to mobility, (c) the ratio of transverse diffusivity to mobility, and (d) the reduced ionization coefficient. The error bar, if available, indicates the reported standard deviation of the measurement.

to be radiatively de-excited to $1s$ -levels based on radiative transition probabilities [89]. This approximation has been used for comparison with the experiment [6, 35, 68].

2.2.2. Implicit, inter-dependent swarm-analysis datasets The cross section datasets from swarm analysis are, however, not readily usable for quantifying uncertainty in the cross sections. First of all, the cross sections are calibrated in a least-square sense, and the uncertainties in the experiments are not backward-propagated toward the cross sections. Thus, most sources only provide the maximum-likelihood estimate of the cross section and do not attempt to assess its uncertainty. To our knowledge, the only swarm-analysis dataset which does provide its uncertainty is the elastic momentum-transfer

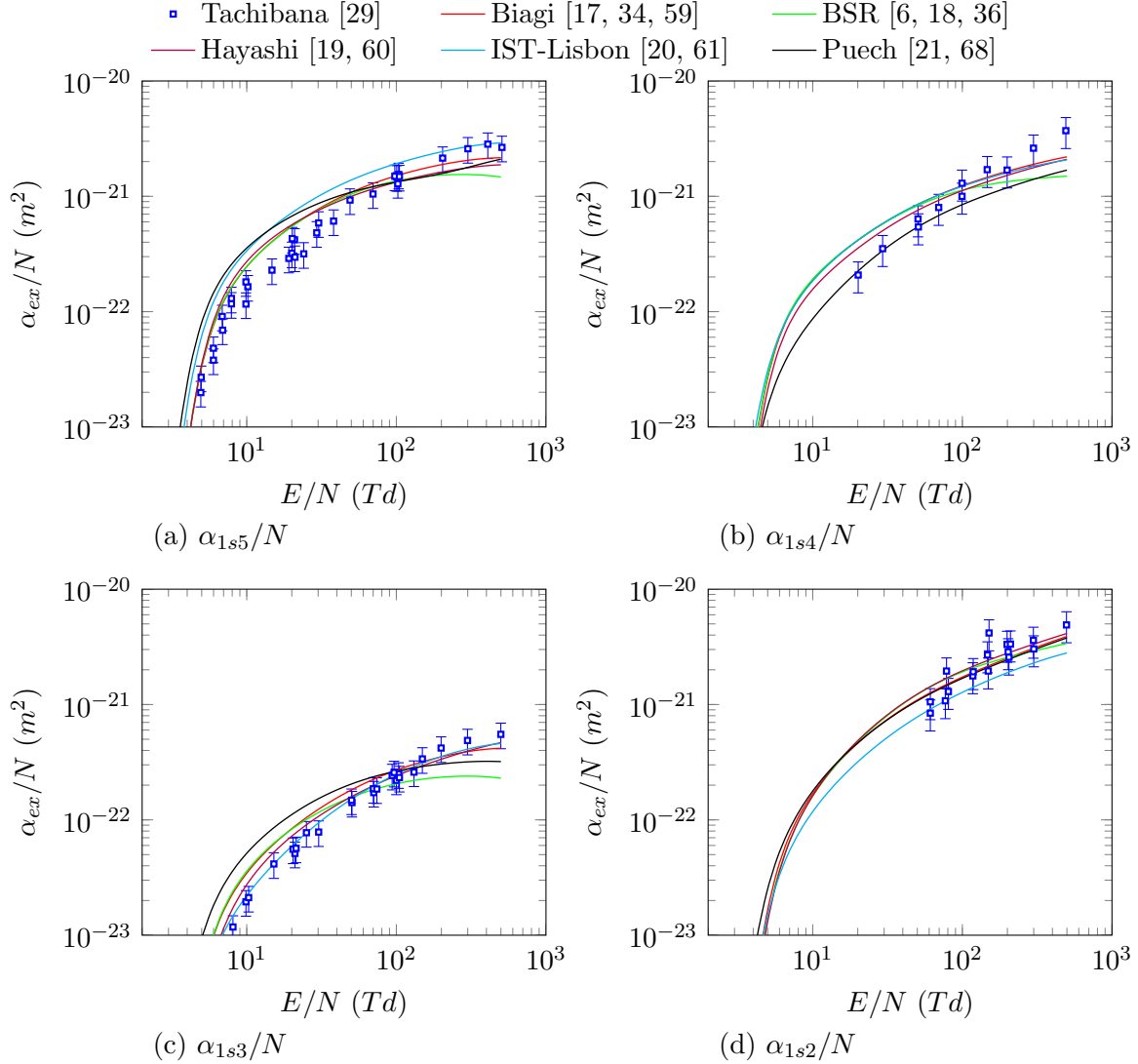


Figure 3. Swarm parameter data used for validation of the calibrated cross sections: the reduced excitation coefficient to the level (a) $1s_5$, (b) $1s_4$, (c) $1s_3$, and (d) $1s_2$. The error bar, if available, indicates the reported standard deviation of the measurement.

cross section at low energy by Milloy *et al.* [31], where the uncertainty is estimated via a sensitivity analysis.

A more fundamental challenge in using these datasets lies in their inter-dependency. The swarm parameters depend on the electron distribution function, which is determined by the entire set of collision processes. The set of collision processes that can be inferred from the transport/chemistry data is not unique, unless the experimental condition reduces the number of possible collision processes [1, 90]. This is possible only for the elastic momentum-transfer processes in the low-energy range for noble gases [1, 31, 90]. A common practice for other collision processes is to calibrate only a target collision process, while the other necessary cross sections are taken from the literature, sometimes with mild adjustments. As a result, the cross sections from swarm

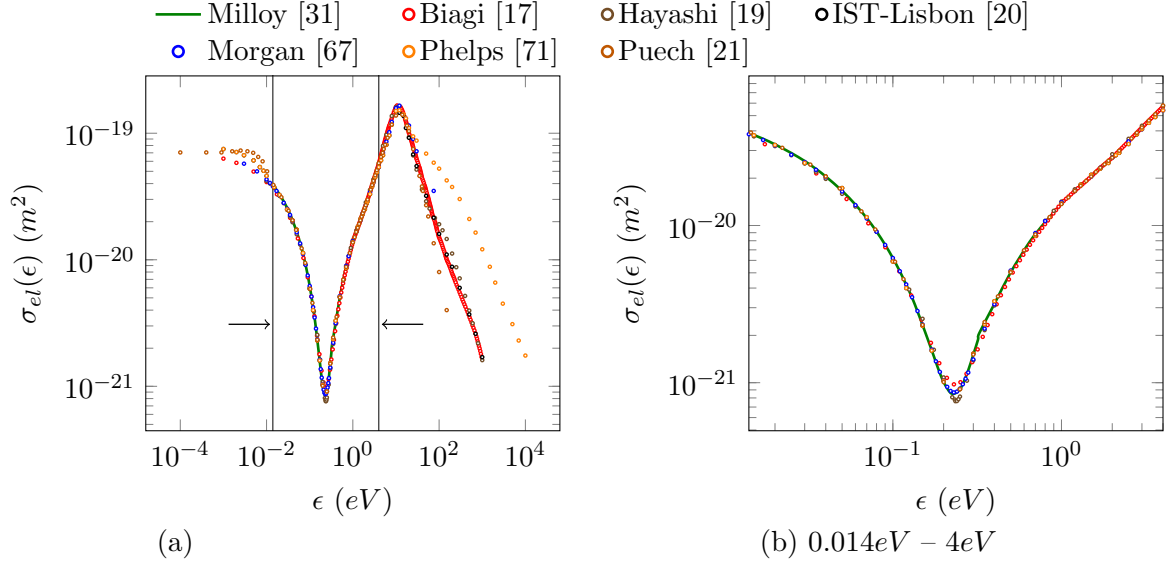


Figure 4. Elastic momentum-transfer cross sections from swarm-analysis datasets: (a) on the overall energy range, and (b) on $\epsilon \in [0.014, 4]$ (eV), to show the agreement with the data from Milloy *et al.* [31].

analysis datasets often show small discrepancies among each other, though this result does not necessarily imply that the actual uncertainty is small. The elastic momentum-transfer cross section shown in Figure 4 is one stark example. While these datasets are mildly scattered either for $\epsilon < 0.014$ eV or for $\epsilon > 4$ eV , all of them are strikingly well aligned within $\epsilon \in [0.014, 4]$ interval, except a small variation at the Ramsauer minimum. While it may be tempting to say that the cross section in this range has an extremely low uncertainty, it is rather the result of everyone adopting and mildly adjusting the dataset from Milloy *et al.* [31]. Table 2 shows these swarm-analysis datasets which are known to have adopted Milloy *et al.* [31] with mild adjustments. Employing all these datasets independently will induce a strong, artificial bias to that from Milloy *et al.* [31]. While the elastic collision may be considered accurate on this range, almost all other cross sections—which are not deemed accurate as the momentum-transfer—are also adopted from the literatures as shown in Table 2, thus having an inter-dependency with each other.

For these reasons, the cross sections from swarm-analysis are not used for calibration in this work.

2.2.3. Swarm-parameter experiments as a validation case In principle, the swarm parameter experiment data in Table 3 can be also used for Bayesian inference. This requires an inverse problem of finding the semi-empirical cross section models, whose outputs through the Boltzmann equation match the swarm parameter measurements. This is in essence a more comprehensive swarm-analysis: the entire set of cross sections would be calibrated together; and the associated uncertainty would be evaluated, which

involves much larger statistical sampling than simply fitting the models, even with a simplified Boltzmann model such as BOLSIG+ [16].

In order to avoid this increase in the sampling cost, it is decided to use only the direct cross section measurements in Table 1 for the Bayesian inference procedure. The swarm parameter experiment data in Table 3 are instead used for validation of the calibrated models resulting from the Bayesian inference, as shown in Section 5.

3. Semi-empirical cross section models

We observe from Figure 1 that, for the most part, the cross sections vary smoothly in ϵ -space. Thus, while their reported measurement errors might be assumed independent, this assumption certainly does not hold true for the cross section itself. Further, it suggests that the cross section behavior can be adequately described with a low-dimensional parameter set.

To take advantage of this behavior, we represent the cross sections $\sigma(\epsilon)$ with semi-empirical models $f(\epsilon; \vec{A})$, where \vec{A} denotes the parameters of the model. The parametric uncertainty for \vec{A} represents the uncertainty of the cross section. The semi-empirical models are based on theoretical arguments combined with a few empirical factors [1, 32, 43, 44]. These model forms are intended to capture the essential features of the cross section using a relatively low-dimensional set of uncertain parameters.

While some cross sections—excitations in particular—exhibit rich fine-scale structures [36, 58], most datasets do not have the resolution necessary to support inference of these features. Further, the plasma transport and reaction properties that are the primary quantities of interest in this work are integrals over energy, and are therefore insensitive to these fine features in the cross sections. This insensitivity is demonstrated via sensitivity analysis in Appendix A. Thus, even when some small-scale features are present—and thus a richer model would be necessary to capture these features—we rely upon low-dimensional, semi-empirical models.

3.1. Elastic momentum-transfer

For low electron-impact energy ($< 1\text{eV}$), the modified effective range theory (MERT) model has been widely used for the elastic momentum-transfer cross section [31, 32, 91]. The cross section is expressed as partial wave expansions,

$$f_{MERT}(\epsilon; \vec{A}_{MERT}) = \frac{4\pi}{k^2} \sum_{L=0}^{\infty} \sin^2(\eta_L - \eta_{L+1}), \quad (1a)$$

where $k^2 = (2m_e/\hbar^2)\epsilon$ with the electron mass m_e and the reduced Planck constant \hbar . The MERT formula determines the electron-atom scattering phase shift η_L with 4 empirical factors $\vec{A}_{MERT} = \{A, D, F, \epsilon_1\}$,

$$k^{-1} \tan \eta_0 = -A \left[1 + \frac{4\alpha}{3a_0} k^2 \log(ka_0) \right] - \frac{\pi\alpha}{3a_0} k^2 + Dk^3 + Fk^4, \quad (1b)$$

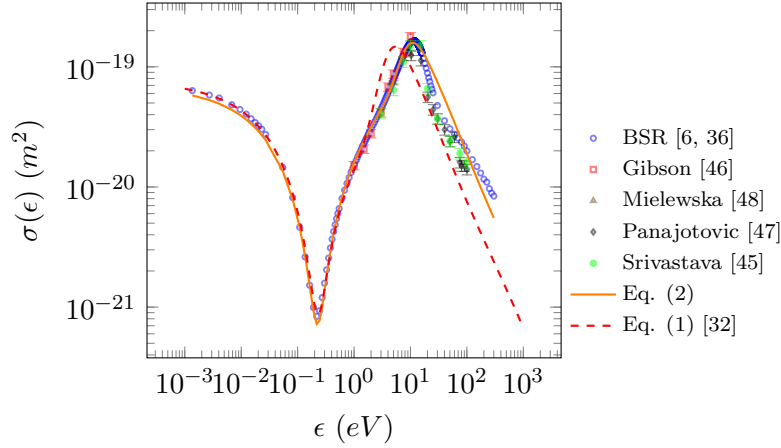


Figure 5. The semi-empirical model (2) for the elastic momentum-transfer cross section, together with the electron-beam experiment datasets. The MERT model (1) by Haddad and O'Malley [32] is also included for a reference.

$$k^{-1} \tan \eta_1 = \frac{\pi}{15} \alpha k \left(1 - \sqrt{\frac{\epsilon}{\epsilon_1}} \right) \quad (1c)$$

$$k^{-1} \tan \eta_L = \frac{\pi \alpha k}{(2L+3)(2L+1)(2L-1)a_0} \quad \text{for } L > 1, \quad (1d)$$

with $a_0 = 5.29177 \times 10^{-11} m$ the Bohr radius and $\alpha = 11.08a_0^3$ the static polarizability of argon atom. Figure 5 shows the MERT model calibrated by Haddad and O'Malley [32], which agrees well with BSR calculation up to 1eV and deviates from the electron-beam experiment data for the larger energy range.

We note that, while the MERT model deviates for $> 1eV$, it exhibits a qualitatively similar trend with the electron-beam data, and that it only requires a minor shift along ϵ -axis. Thus we designed an extension to the MERT model,

$$f_{el}(\epsilon; \vec{A}_{el}) = f_{MERT}(\tilde{\epsilon}; \vec{A}_{MERT}), \quad (2a)$$

where $\vec{A}_{el} = \{\vec{A}_{MERT}, t_1, t_2, t_3\}$ includes three additional parameters, which are used to determine the shift factor applied to ϵ ,

$$\tilde{\epsilon} = \epsilon \left[\frac{1+t_1}{2} - \frac{1-t_1}{2} \tanh \left(\frac{\epsilon - t_2}{t_3} \right) \right]. \quad (2b)$$

In essence, (2b) amplifies ϵ by a factor of t_1 if $\epsilon > t_2$. Figure 5 shows the model with \vec{A}_m least-square-fitted against the BSR dataset, which seems flexible enough to capture the overall trend of the momentum-transfer cross section. This model approximates the high-energy ($> 10eV$) range with only $\mathcal{O}(\epsilon^{-1})$ asymptote, neglecting smaller-scale variations. However, a sensitivity analysis using a zero-dimensional Boltzmann solver (BOLSIG+ [16]) indicated that the resulting swarm parameters are insensitive to these variations (see Appendix A).

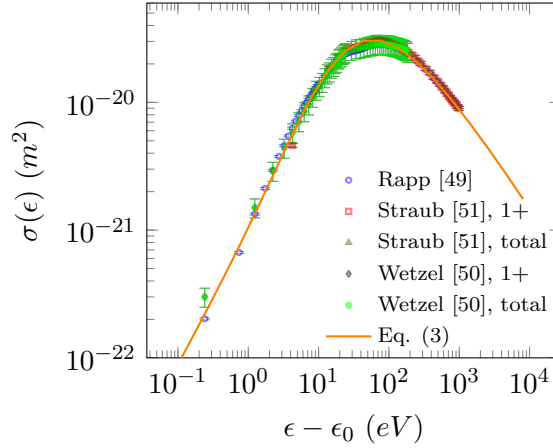


Figure 6. The semi-empirical model (3) for the total ionization cross section, together with the electron-beam experiment datasets.

3.2. Ionization

Kim and Rudd [1, 44] suggested a simple empirical form for the total ionization cross section based on the binary-encounter-dipole model,

$$f_i(\epsilon; \vec{A}_i) = \frac{4\pi a_0^2}{\epsilon/\epsilon_i} \left[a \log \frac{\epsilon}{\epsilon_i} + b \left(1 - \frac{\epsilon_i}{\epsilon} \right) + c \frac{\log(\epsilon/\epsilon_i)}{\epsilon/\epsilon_i + 1} \right], \quad (3)$$

with $\epsilon_i = 15.760\text{eV}$ the first ionization energy of argon and $\vec{A}_i = \{a, b, c\}$ the model parameters for f_i . Figure 6 shows the empirical model evaluated using least-squares-fitted parameters, compared with the electron-beam datasets.

3.3. Excitation—metastables

For $1s_5$, $1s_3$ excitation cross sections, we employ a semi-empirical model suggested by Bretagne *et al.* [43],

$$f_{me}(\epsilon; \vec{A}_{me}) = \frac{4\pi a_0^2 R}{\epsilon} b_{me} \left(1 - \frac{\epsilon_{me}}{\epsilon} \right) (2\epsilon)^{-\gamma_{me}}, \quad me = 1s_5, 1s_3, \quad (4)$$

with $R = 13.606\text{eV}$ the Rydberg energy, $\epsilon_{1s5} = 11.548\text{eV}$, $\epsilon_{1s3} = 11.723\text{eV}$ the excitation energies for $1s_5$ and $1s_3$ levels, respectively, and the model parameters $\vec{A}_{me} = \{b_{me}, \gamma_{me}\}$. The first term in (4) corresponds to the large-energy asymptotic limit from Bethe-Born approximation, while the last two terms are the empirical factors for the low-energy range. Figure 7 shows the models with the literature values from Bretagne *et al.* [43]. The trends agree well with the measurement data. The model, of course, cannot capture the fine resonance structures [58] and the small-scale behaviors for $\epsilon - \epsilon_0 < 10^{-1}\text{eV}$, which are observed in the BSR dataset. A small sensitivity analysis via BOLSIG+ [16], however, revealed that the plasma chemistry and transport properties are insensitive to these fine features (see Appendix A).

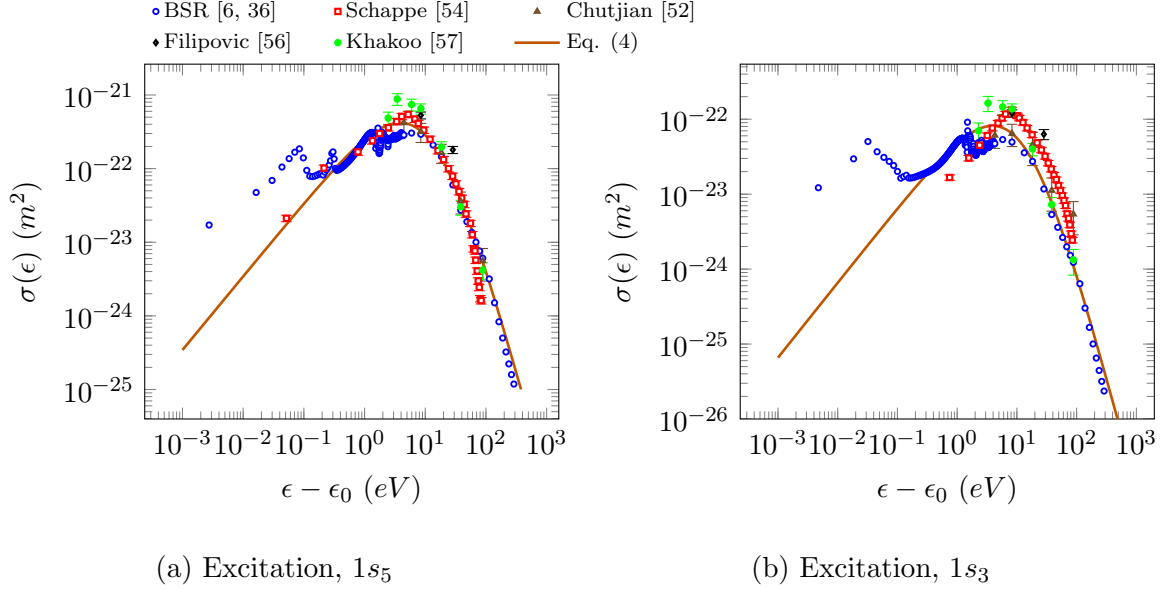


Figure 7. The semi-empirical model (4) for the (a) $1s_5$ and (b) $1s_3$ level excitation cross section, together with the electron-beam experiment datasets.

3.4. Excitation—resonances

For resonance level excitations $1s_4$ and $1s_2$, we employ a similar model to that from Bretagne *et al.* [43] which accounts for the relativistic effect for electrons,

$$f_r(\epsilon; \vec{A}_r) = \frac{4\pi a_0^2 R^2}{\epsilon} \frac{F_{0,r}}{\epsilon_r} \left[\log \left(\frac{\epsilon}{(1 - \beta^2)\epsilon_r} \right) - \beta^2 \right] \exp \left[-\frac{\gamma_r}{1 + \epsilon/\epsilon_r} \right], \quad r = 1s_4, 1s_2, \quad (5)$$

where $\beta = \sqrt{2\epsilon/m_e c^2}$ the relativistic factor with the electron mass m_e and the speed of light c , and the model parameters $\vec{A}_r = \{F_{0,r}, \gamma_r\}$. The excitation energies $\epsilon_{1s4} = 11.624\text{eV}$ and $\epsilon_{1s2} = 11.828\text{eV}$ are chosen from the NIST atomic spectra database [92]. The difference of (5) from the model by Bretagne *et al.* [43] is the last empirical factor, which adjusts the low-energy behavior. This adjustment is similar to the low-energy empirical factor suggested by Paretzke [1]. Figure 8 shows results using reference parameter values. The qualitative trends agree well with the measurement data.

4. Uncertainty quantification via Bayesian inference

4.1. Overall framework

We represent the uncertainty of a cross section $\sigma(\epsilon)$ with the parametric uncertainty of the corresponding semi-empirical model $f(\epsilon; \vec{A})$ calibrated with the given measurement data \mathcal{M} . Specifically, this information is encoded in the probability distribution $P[\vec{A}|\mathcal{M}]$, which is the distribution for the model parameters conditioned on the observations in \mathcal{M} . As shown in Figure 1, each cross section has corresponding

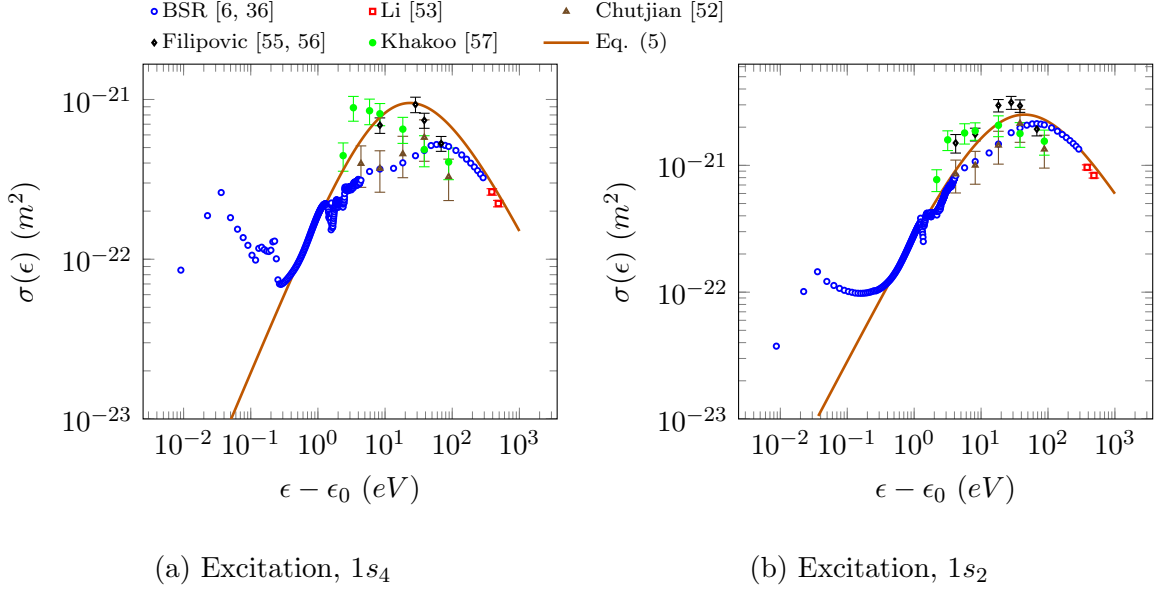


Figure 8. The semi-empirical model (4) for the (a) $1s_4$ and (b) $1s_2$ level excitation cross section, together with the electron-beam experiment datasets.

measurement data \mathcal{M} composed of multiple datasets,

$$\mathcal{M} = \{\mathcal{M}_1, \mathcal{M}_2, \dots, \mathcal{M}_M\}. \quad (6a)$$

Each dataset \mathcal{M}_m consists of data points $(\vec{\epsilon}_m, \vec{\sigma}_m)$ and reported measurement uncertainties $\Delta\vec{\sigma}_m$,

$$\mathcal{M}_m = (\vec{\epsilon}_m, \vec{\sigma}_m, \Delta\vec{\sigma}_m), \quad m = 1, \dots, M, \quad (6b)$$

where $\vec{\epsilon}_m, \vec{\sigma}_m, \Delta\vec{\sigma}_m \in \mathbb{R}^{N_m}$, and N_m denotes the number of data points in the dataset \mathcal{M}_m .

According to the Bayes' law, the desired parametric uncertainty $P[\vec{A}|\mathcal{M}]$ is

$$\underbrace{P[\vec{A}|\mathcal{M}]}_{\text{posterior}} \propto \underbrace{P[\mathcal{M}|\vec{A}]}_{\text{likelihood}} \underbrace{P[\vec{A}]}_{\text{prior}}. \quad (7)$$

The prior distribution $P[\vec{A}]$ is a probabilistic representation of any information about the parameters \vec{A} that is available separate from the data \mathcal{M} . For given parameters \vec{A} , the likelihood $P[\mathcal{M}|\vec{A}]$ is the probability distribution for the measurements conditioned on \vec{A} . For given data \mathcal{M} , the likelihood is a function of \vec{A} that encodes the logic that values for \vec{A} that make the observed values of the measurements a more probable outcome of the model should be favored over parameter values that make the observations less likely, all other things being equal.

The formulation of the right-hand side of (7) is not unique. That is, in most complicated problems at least, there are not clearly establishable, true distributions for the prior and likelihood. Instead, these distributions are mathematical models that represent a given state of information. Different models could reflect, for instance,

different interpretations of the data or different hypotheses about the nature of the important uncertainties. Thus, the formulation can differ depending on what uncertain factors are considered and how they are modeled.

To illustrate this fact and the implications of different choices, three likelihood formulations are introduced below. In Section 4.2, we introduce the simplest likelihood formulation that only considers the measurement uncertainty. An alternative formulation is provided in Section 4.3, where the systematic error is also considered as a type of parametric uncertainty. Lastly in Section 4.4, we propose a likelihood formulation where the systematic error is not absorbed into the cross section model parameters. It will be shown in Section 5 that this approach is most appropriate in the present setting, while the first two can lead to misleading conclusions.

4.2. A likelihood formulation with the measurement error only

We first consider the reported measurement errors as the only uncertainty. With the assumption that each dataset is obtained independently, the resulting likelihood of the overall data \mathcal{M} is

$$P_1 [\mathcal{M}|\vec{A}] = \prod_{m=1}^M P_1 [\mathcal{M}_m|\vec{A}], \quad (8)$$

where a subscript for P is used to discern different likelihoods. For the n -th data point $(\epsilon_{m,n}, \sigma_{m,n})$ in a dataset \mathcal{M}_m , we consider a *measurement* model with a multiplicative measurement error $\delta\sigma_{m,n}$,

$$\sigma_{m,n} = f(\epsilon_{m,n}; \vec{A}) \times \delta\sigma_{m,n}, \quad (9)$$

so that

$$\log \sigma_{m,n} = \log f(\epsilon_{m,n}; \vec{A}) + \log \delta\sigma_{m,n}. \quad (10)$$

We assume the logarithm of the measurement error $\log \delta\vec{\sigma}_m$ follows an independent Gaussian distribution based on the reported relative error,

$$P(\log \delta\vec{\sigma}_m) = \mathcal{N} \left[0, \text{diag} \left(\log^2 \left(1 + \frac{\Delta\vec{\sigma}_m}{\vec{\sigma}_m} \right) \right) \right], \quad (11)$$

where all arithmetic operations between vectors are element-wise. This logarithmic scale model is justified by the fact that the majority of the measurement data report their accuracy in terms of the relative error $\Delta\vec{\sigma}/\vec{\sigma}$. While the BSR dataset does not report the accuracy of the dataset, we imposed a 10% relative error based on its credibility as described in Section 2.1. With the probability model (11), the likelihood of a dataset \mathcal{M}_m based on (10) is

$$P_1 [\mathcal{M}_m|\vec{A}] = \mathcal{N} \left[\log f(\vec{\epsilon}_m; \vec{A}), \text{diag} \left(\log^2 \left(1 + \frac{\Delta\vec{\sigma}_m}{\vec{\sigma}_m} \right) \right) \right]. \quad (12)$$

The prior $P(\vec{A})$ is imposed based on any prior knowledge about the collision cross section models. For the total ionization cross section, there is no reported value for

\vec{A}_i , and therefore the uniform prior $P(\vec{A}_i) = 1$ is imposed. For the elastic momentum-transfer collision, a Gaussian probability is imposed on \vec{A}_{MERT} based on the literature value from Haddad and O'Malley [32] with 50% relative standard deviation,

$$P(\vec{A}_{el}) = P(\vec{A}_{MERT}) = \mathcal{N} \left[\vec{A}_{MERT,ref}, \text{diag} \left((0.5 \vec{A}_{MERT,ref})^2 \right) \right], \quad (13)$$

with $\vec{A}_{MERT,ref} = \{-1.488, 65.4, -84.3, 0.983\}$. For the metastable-level excitation cross sections, a Gaussian probability is imposed on \vec{A}_{me} based on the literature values from Bretagne *et al.* [43] with 100% relative standard deviation,

$$P(\vec{A}_{me}) = \mathcal{N} \left[\vec{A}_{me,ref}, \text{diag} \left(\vec{A}_{me,ref}^2 \right) \right], \quad (14)$$

with $\vec{A}_{1s5} = \{51.2, 2.0\}$ and $\vec{A}_{1s3} = \{10.4, 2.0\}$. For the resonance-level excitation cross sections, a Gaussian probability is imposed on $F_{0,r}$ based on the literature values from Bretagne *et al.* [43] with 100% relative standard deviation,

$$P(\vec{A}_r) = P(F_{0,r}) = \mathcal{N} \left[F_{0,r,ref}, F_{0,r,ref}^2 \right], \quad (15)$$

with $F_{0,1s4,ref} = 0.061$ and $F_{0,1s2,ref} = 0.254$.

To examine how the data impacts the uncertainty of \vec{A} under this formulation, we consider two cases. In the first, each data set is used individually, so that the posterior is given by

$$P_1 \left[\vec{A} | \mathcal{M}_m \right] \propto P_1 \left[\mathcal{M}_m | \vec{A} \right] P(\vec{A}), \quad (16)$$

with the individual likelihood (12) and the priors (13–15). In the second, all the data are used simultaneously, so that

$$P_1 \left[\vec{A} | \mathcal{M} \right] \propto \prod_{m=1}^M P_1 \left[\mathcal{M}_m | \vec{A} \right] P(\vec{A}), \quad (17)$$

with the overall likelihood (8) and the same priors (13–15).

4.3. All systematic error represented as the parametric uncertainty

In Section 2, we note that the measurement data \mathcal{M} exhibits a large scattering among the datasets \mathcal{M}_m which is much larger than their reported observation errors $\Delta \vec{\sigma}_m$. This systematic error may not be negligible and thus should be accounted for in the probabilistic model using in the inference process. One approach is to model the systematic error as an additional parametric uncertainty, so each dataset \mathcal{M}_m may have a disturbance $\delta \vec{A}_m$ in its parameter value,

$$\vec{A}_m = \vec{A} + \delta \vec{A}_m. \quad (18)$$

This disturbance may be modeled to follow a joint Gaussian distribution over the parameter \vec{A} -space with a covariance,

$$P_2 \left[\delta \vec{A}_m | \vec{\theta} \right] = \mathcal{N} \left[\vec{0}, \Sigma(\vec{\theta}) \right], \quad (19)$$

where, considering the symmetry of the covariance, $\vec{\theta}$ corresponds to all the entries of the upper-triangular part of Σ . Aside from the true \vec{A} , several additional variables are considered uncertain in this viewpoint: $\{\vec{A}_m\}_{m=1}^M$ the realizations of \vec{A} for all datasets and the model parameter $\vec{\theta}$. The Bayes' law (7) then should reflect all the uncertain variables, having the resulting joint posterior,

$$\begin{aligned} P_2 \left[\vec{A}, \vec{\theta}, \{\vec{A}_m\}_{m=1}^M | \mathcal{M} \right] &\propto P_2 \left[\mathcal{M}, \{\vec{A}_m\}_{m=1}^M | \vec{A}, \vec{\theta} \right] P[\vec{A}] P_2[\vec{\theta}] \\ &\propto \prod_{m=1}^M P_2 \left[\mathcal{M}_m | \vec{A}_m, \vec{A}, \vec{\theta} \right] P_2 \left[\vec{A}_m | \vec{A}, \vec{\theta} \right] P[\vec{A}] P_2[\vec{\theta}]. \end{aligned} \quad (20)$$

For the cross section model parameter \vec{A} as our primary interest, we consider all possibilities for $\{\vec{A}_m\}_{m=1}^M$ and $\vec{\theta}$ and thus marginalize $P_2 \left[\vec{A}, \vec{\theta}, \{\vec{A}_m\}_{m=1}^M | \mathcal{M} \right]$ over $\{\vec{A}_m\}_{m=1}^M$ and $\vec{\theta}$,

$$P_2 \left[\vec{A} | \mathcal{M} \right] = \int P_2 \left[\vec{A}, \vec{\theta}, \{\vec{A}_m\}_{m=1}^M | \mathcal{M} \right] d\vec{\theta} d\vec{A}_1 \cdots d\vec{A}_M. \quad (21)$$

With (18) and (19), the likelihood for \vec{A}_m is

$$P_2 \left[\vec{A}_m | \vec{A}, \vec{\theta} \right] = \mathcal{N} \left[\vec{A}, \Sigma(\vec{\theta}) \right]. \quad (22)$$

When the parameter is realized as \vec{A}_m in the measurement m , the likelihood of the dataset \mathcal{M}_m is

$$P_2 \left[\mathcal{M}_m | \vec{A}_m, \vec{A}, \vec{\theta} \right] = \mathcal{N} \left[\log f(\vec{\epsilon}_m; \vec{A}_m), \text{diag} \left(\log^2 \left(1 + \frac{\Delta \vec{\sigma}_m}{\vec{\sigma}_m} \right) \right) \right], \quad (23)$$

which is similar to (12) but the expected cross section is based on \vec{A}_m .

The same priors (13–15) are used for $P[\vec{A}]$. For the systematic error model parameter $\Sigma(\vec{\theta})$, there is little information available to inform the probability for $\vec{\theta}$, and we can only expect that the corresponding variances would not be extremely small or large compared to the parameter value itself. Thus we assume the corresponding variances to be uniform on the logarithmic scale,

$$P_2[\vec{\theta}] = \prod_{d=1}^{\dim(\Sigma)} P_2 \left[V_d(\vec{\theta}) \right] \quad (24a)$$

$$P_2 \left[V_d(\vec{\theta}) \right] = \begin{cases} \frac{1}{V_d(\log V_{d,max} - \log V_{d,min})} & V_d \in [V_{d,min}, V_{d,max}] \\ 0 & \text{otherwise,} \end{cases} \quad (24b)$$

with $V_d(\vec{\theta})$ the variance along the d -th principal axis of $\Sigma(\vec{\theta})$ and $V_{d,min} = 10^{-2}$ and $V_{d,max} = 10^1$. In actual evaluation, V_d is determined as the d -th singular value of $\Sigma(\vec{\theta})$ given the parameter $\vec{\theta}$. The posterior (21) is then evaluated with (20), (23), (13–15) and (24).

This description is predicated upon a strong assumption that the model-form error is negligible and that systematic differences between the experiments are due to each separate experiment realizing different values of the semi-empirical model parameters. It shall be seen in Section 5 how this assumption impacts the results for \vec{A} .

4.4. A probabilistic description with a model for the systematic error

While the measurement data \mathcal{M} exhibits a systematic error among the datasets \mathcal{M}_m , the employed semi-empirical models also do not necessarily capture all the features at all scales. For example, the BSR excitation cross sections in Figure 1 (c–f) exhibits small-scale variations near $\epsilon - \epsilon_0 \sim 1\text{eV}$, which cannot be represented at all by the model forms introduced in Section 3. Thus, in addition to the systematic errors in the data, a model-form error is present. The combined effect of the systematic data errors and the model inadequacies is denoted by δf here. Specifically, similar to (9), we consider a measurement model for the n -th data point $(\epsilon_{m,n}, \sigma_{m,n})$ in a dataset \mathcal{M}_m , where δf , which depends on additional parameters denoted $\vec{\theta}$, appears as an additional multiplicative factor,

$$\sigma_{m,n} = f(\epsilon_{m,n}; \vec{A}) \times \delta f(\epsilon_{m,n}; \vec{\theta}) \times \delta \sigma_{m,n}, \quad (25)$$

which implies that

$$\log \sigma_{m,n} = \log f(\epsilon_{m,n}; \vec{A}) + \log \delta f(\epsilon_{m,n}; \vec{\theta}) + \log \delta \sigma_{m,n}. \quad (26)$$

The resulting joint posterior analogous to (20) is

$$P_3 [\vec{A}, \vec{\theta} | \mathcal{M}] \propto P_3 [\mathcal{M} | \vec{A}, \vec{\theta}] P [\vec{A}] P_3 [\vec{\theta}], \quad (27)$$

where the parameters \vec{A} and $\vec{\theta}$ are taken to be independent in the prior. Similar to (21), we consider all possibilities for $\vec{\theta}$ and thus marginalize $P [\vec{A}, \vec{\theta} | \mathcal{M}]$ over $\vec{\theta}$,

$$P_3 [\vec{A} | \mathcal{M}] \propto \int P_3 [\mathcal{M} | \vec{A}, \vec{\theta}] P [\vec{A}] P_3 [\vec{\theta}] d\vec{\theta}. \quad (28)$$

With the assumption that each dataset is obtained independently, the resulting likelihood of the overall data \mathcal{M} is

$$P_3 [\mathcal{M} | \vec{A}, \vec{\theta}] = \prod_{m=1}^M P_3 [\mathcal{M}_m | \vec{A}, \vec{\theta}], \quad (29)$$

where $P_3 [\mathcal{M}_m | \vec{A}, \vec{\theta}]$ will be determined from (26) with the uncertainty models for $\log \delta \vec{\sigma}_m$ and $\delta f(\epsilon; \vec{\theta})$.

While the same model (11) is used for the measurement uncertainty $\log \delta \vec{\sigma}_m$, modeling $\delta f(\epsilon; \vec{\theta})$ requires further development. Unlike the cross section itself, it is difficult to model the discrepancy as a simple analytical function as $f(\epsilon; \vec{A})$. As

described in Section 2, there are many potential factors involved in the discrepancy among datasets, each of which is hard to quantify. This is further aggravated by the fact that we have no knowledge to separate the model inadequacy from the systematic error so that they may be modeled individually.

In this situation, Gaussian processes (GP) provide a flexible probabilistic framework for representing the observed combined effects of these errors. Specifically, for a given $\vec{\theta}$ and a dataset \mathcal{M}_m , we model $\log \delta f(\vec{\epsilon}_m)$ as a Gaussian random function with zero mean and covariance $\mathbf{K}(\vec{\epsilon}_m, \vec{\epsilon}_m; \vec{\theta}) \in \mathbb{R}^{N_m \times N_m}$,

$$P_3 \left[\log \delta f(\vec{\epsilon}_m) \mid \vec{\theta} \right] = \mathcal{N} \left[\vec{0}, \mathbf{K}(\vec{\epsilon}_m, \vec{\epsilon}_m; \vec{\theta}) \right]. \quad (30)$$

Each entry of the covariance matrix is determined by the covariance kernel k ,

$$\mathbf{K}(\vec{\epsilon}_m, \vec{\epsilon}_m; \vec{\theta})_{ij} = k(d_{m,ij}; \vec{\theta}), \quad (31)$$

where $d_{m,ij}$ the distance between two data points $\epsilon_{m,i}$ and $\epsilon_{m,j}$ is determined in the logarithmic scale, based on the scaling behavior of each collision cross section. For the elastic cross section,

$$d_{m,ij} = |\log \epsilon_{m,i} - \log \epsilon_{m,j}|, \quad (32a)$$

and for the other collisions with threshold energy ϵ_0 ,

$$d_{m,ij} = |\log(\epsilon_{m,i} - \epsilon_0) - \log(\epsilon_{m,j} - \epsilon_0)|. \quad (32b)$$

The widely used Matérn kernel is used for $k(d; \vec{\theta})$ with model parameters $\vec{\theta} = \{V_\theta, d_\theta\}$,

$$k(d; \vec{\theta}) = V_\theta \frac{2^{1-\nu}}{\Gamma(\nu)} \left(\sqrt{2\nu} \frac{d}{d_\theta} \right)^\nu K_\nu \left(\sqrt{2\nu} \frac{d}{d_\theta} \right), \quad (33)$$

where Γ is the gamma function, K_ν is the modified Bessel function of the second kind, and $\nu = 1.5$. V_θ and d_θ are the main parameters of the Matérn kernel that represent the variance and correlation scale, respectively.

With the probability models (30) and (11), the likelihood of a dataset \mathcal{M}_m based on (26) is

$$\begin{aligned} P_3 \left[\mathcal{M}_m \mid \vec{A}, \vec{\theta} \right] &= P_3 \left[\log \vec{\sigma}_m \mid \vec{A}, \vec{\theta} \right] \\ &= \mathcal{N} \left[\log \delta f(\vec{\epsilon}_m; \vec{A}), \mathbf{K}(\vec{\epsilon}_m, \vec{\epsilon}_m; \vec{\theta}) + \text{diag} \left(\log^2 \left(1 + \frac{\Delta \vec{\sigma}_m}{\vec{\sigma}_m} \right) \right) \right]. \end{aligned} \quad (34)$$

The same priors (13–15) are used for $P[\vec{A}]$. Analogous to (24), for the prior $P_3[\vec{\theta}]$, we assume V_θ to be uniform on the logarithmic scale,

$$P_3[\vec{\theta}] = P_3[V_\theta] = \begin{cases} \frac{1}{V_\theta(\log V_{\theta,max} - \log V_{\theta,min})} & V_\theta \in [V_{\theta,min}, V_{\theta,max}] \\ 0 & \text{otherwise,} \end{cases} \quad (35)$$

with the range $V_{\theta,min} = 10^{-2}$ and $V_{\theta,max} = 10^1$.

The likelihood (29), the priors (13–15) and (35) then constitutes the posteriors (27) and (28) for all 6 collision cross sections.

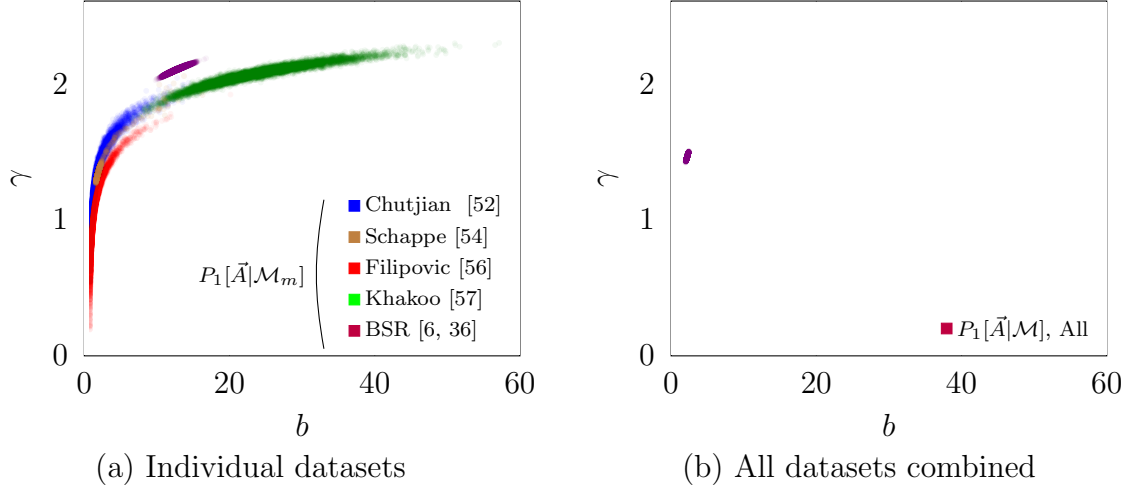


Figure 9. Sample scatter plots of the posterior distributions based on the measurement-uncertainty-only representation (Section 4.2) for $1s_3$ excitation cross section: (a) with individual datasets ($P_1[\vec{A}|\mathcal{M}_m]$ in Eq. 16) and (b) with all datasets combined ($P_1[\vec{A}|\mathcal{M}]$ in Eq. 17).

5. The inferred cross section uncertainty

The probabilistic models from Section 4 are first compared for $1s_3$ excitation cross section as an example, and their implications are discussed. Then the parametric uncertainties of all 6 cross sections are calibrated and presented.

5.1. Comparison of the parametric posterior distributions

The posterior distributions from Section 4 are sampled using a standard Markov chain Monte Carlo (MCMC) algorithm implemented in the `emcee` package [26]. For all posteriors, the total sample size exceeds at least 20 times the auto-correlation length, typically around 50 times, in order to obtain enough effectively independent samples [26].

To illustrate the implication of neglecting the systematic error, all the posteriors described in Section 4.2 are evaluated for the $1s_3$ excitation cross section. Figure 9 (a) shows samples from the posteriors $P_1[\vec{A}|\mathcal{M}_m]$ (16) obtained from individual datasets \mathcal{M}_m . The individual posteriors are scattered in \vec{A} -space, and mostly do not overlap with each other. This again reflects the scattering among the cross section datasets in Figure 1 (e), implying that there is a large uncertainty in the cross section model parameters. When evaluated using all the datasets simultaneously, however, the probability description in Section 4.2 cannot capture this uncertainty. In Figure 9 (b), the overall posterior $P_1[\vec{A}|\mathcal{M}]$ (17) is highly concentrated in a narrow region, indicating a very low uncertainty in \vec{A} . This is obviously a misleading conclusion given the scatter among the individual datasets.

This does not mean that the Bayesian inference is wrong. It is mathematically consistent given the likelihoods (12) and (8). From (12), each dataset \mathcal{M}_m claims a

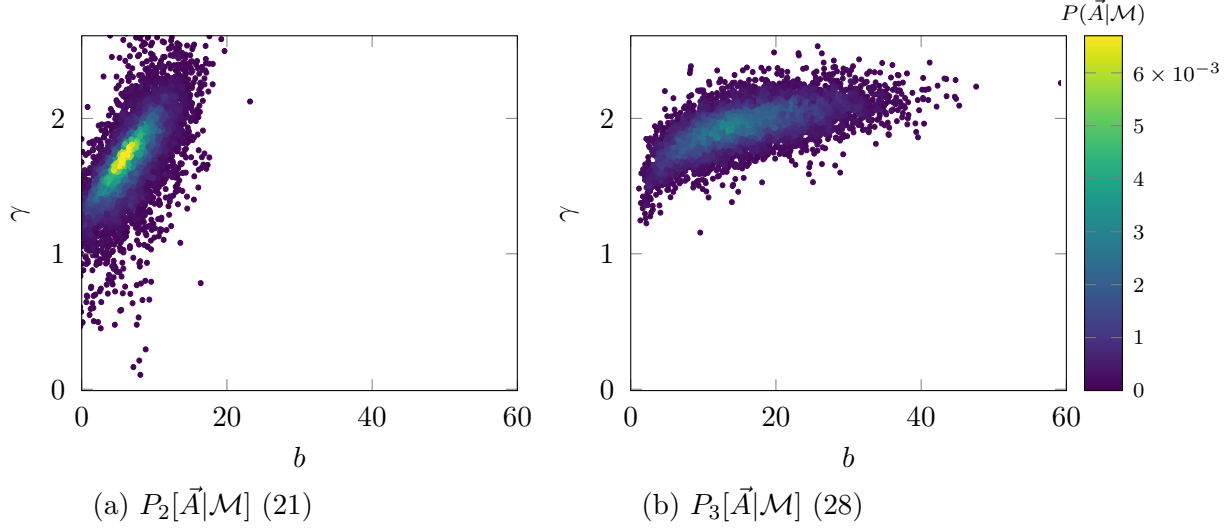


Figure 10. Sample scatter plots of the posterior distributions of $1s_3$ excitation cross section: (a) $P_2[\vec{A}|\mathcal{M}]$ (21) based on the internal parametric uncertainty representation (Section 4.3) and (b) $P_3[\vec{A}|\mathcal{M}]$ (28) based on the Gaussian process representation (Section 4.4). In both figures, samples are colored according to their posterior probability.

different best value of \vec{A} with its own measurement error $\delta\vec{\sigma}_m$. The overall likelihood (8), which is simply the product of the likelihood for each dataset, naturally leads to a concentration of the posterior probability around a value somewhere in the middle. This unrealistic result reflects the fact that the problem statement (10) does not properly account for all sources of uncertainty in the likelihood formulation.

The uncertainty underlying the scattering among datasets can be captured only when it is explicitly considered in the probabilistic description. Figure 10 shows the posterior distributions evaluated with the systematic error models. Whether as an additional parameter uncertainty or as a Gaussian process, considering the possibility of the systematic error significantly increases the uncertainty of \vec{A} . While both posteriors are peaked at similar parameter values, their distributions have qualitatively different shapes. In turn, each systematic error model leads to a different conclusion about the uncertainties of the cross section model parameters: while, with P_2 (21), we may conclude that the uncertainty in (γ, b) follows a Gaussian distribution with the uncertainty in γ more pronounced, P_3 (28) rather seems to conclude that b is more uncertain.

The difference between the two systematic error models appears more drastically when the uncertainty of the cross section $\sigma(\epsilon)$ is considered. Figure 11 shows the distribution of $\sigma(\epsilon)$ obtained by forward propagating each $P[\vec{A}|\mathcal{M}]$ through the parametric model compared to the calibration data. Once again, the results from (17) do not capture the systematic errors among datasets, with the probability concentrated on almost a single line. On the other hand, while the Gaussian process model seems

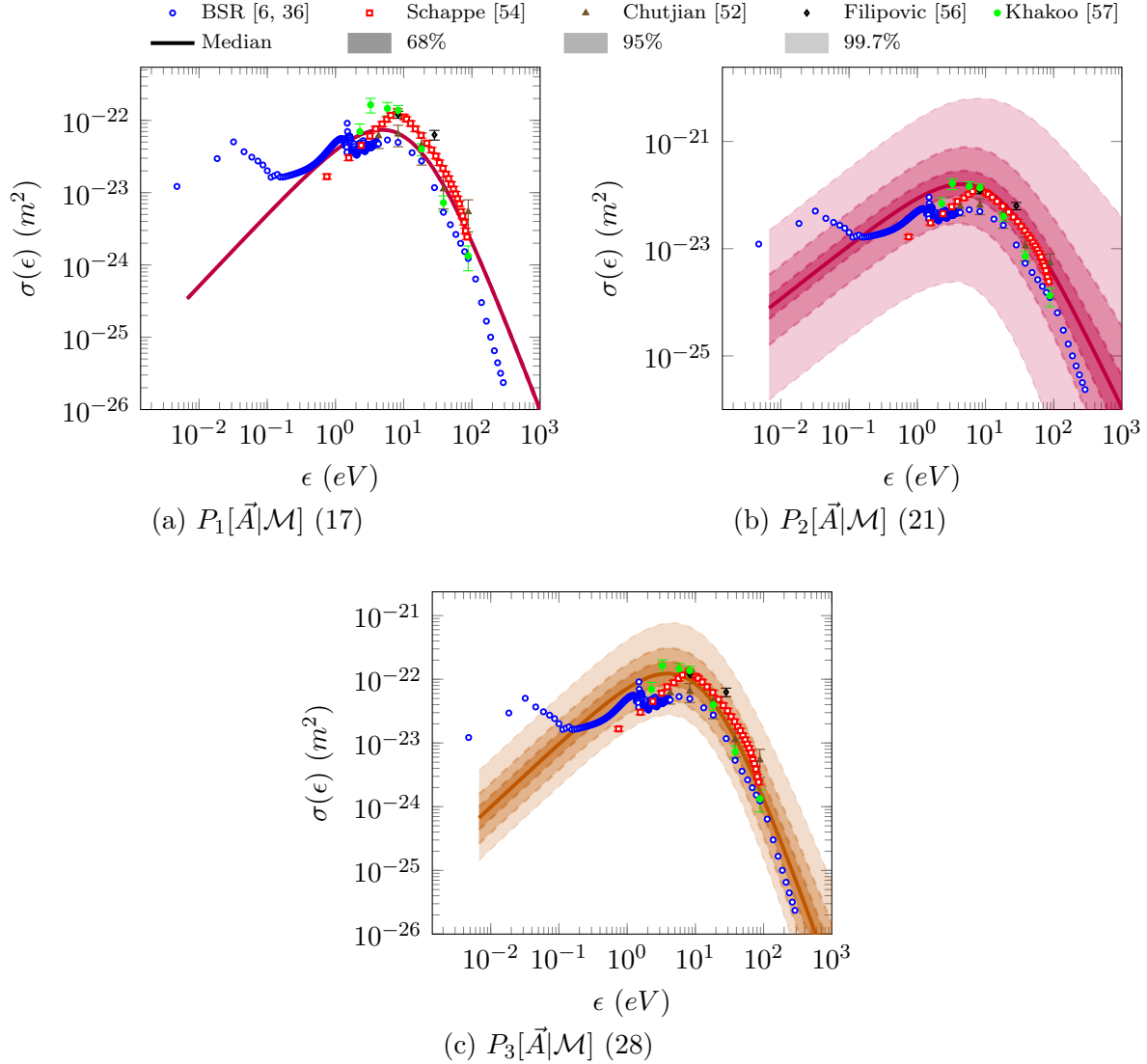


Figure 11. Marginal posterior distribution $P[\sigma(\epsilon)|\mathcal{M}]$ for $1s_3$ excitation cross section with (a) $P_1[\vec{A}|\mathcal{M}]$ (17) based on the measurement-uncertainty-only representation (Section 4.2); (b) $P_2[\vec{A}|\mathcal{M}]$ (21) based on the internal parametric uncertainty representation (Section 4.3); and (c) $P_3[\vec{A}|\mathcal{M}]$ (28) based on the Gaussian process representation (Section 4.4). Shaded areas indicate the 68%, 95% and 99.7% credibility intervals of the posterior distribution.

to properly capture the scattering among the datasets, the resulting posterior from the internal parametric uncertainty model is overly uncertain about \vec{A} , with its credibility intervals exceeding way beyond the measurement datasets. Moreover, considering the median value of the cross section in $\epsilon > 10^2 \text{ eV}$, the internal parametric uncertainty model deviates from the datasets compared to the Gaussian process model, implying a slight miscalibration of the parameter value.

A deeper analysis of the posterior distributions can expose the flaw of the internal

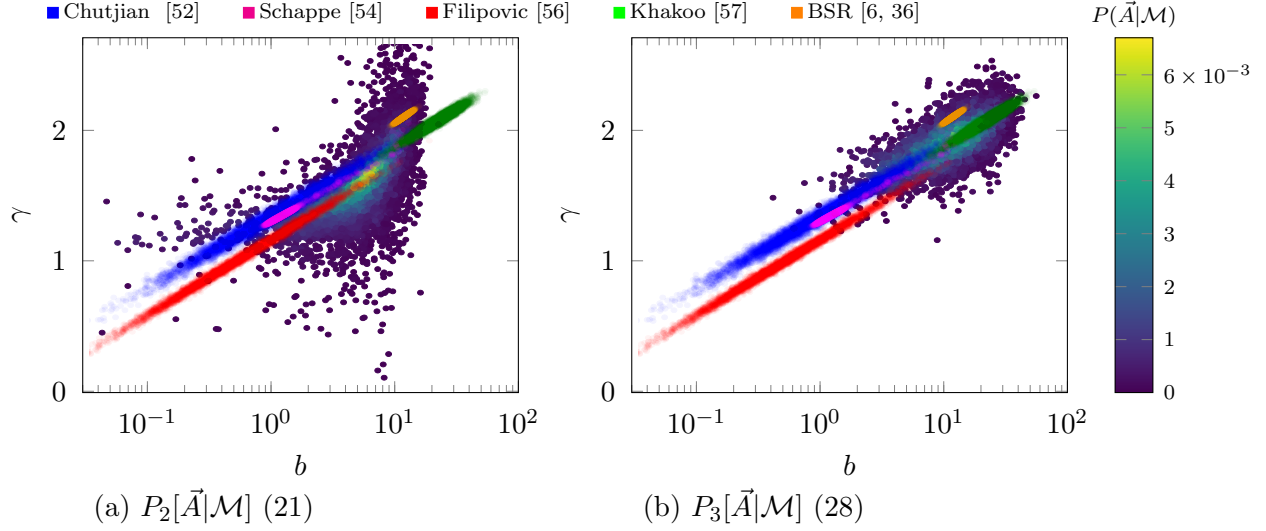


Figure 12. Sample scatter plots of the posterior distributions of $1s_3$ excitation cross section on log scale of b : (a) the internal parametric uncertainty representation $P_2[\vec{A}|\mathcal{M}]$ (Eq. 21 in Section 4.3) and (b) the Gaussian process representation $P_3[\vec{A}|\mathcal{M}]$ (Eq. 28 in Section 4.4) compared with the measurement-uncertainty-only representation of individual datasets $P_1[\vec{A}|\mathcal{M}_m]$ (Eq. 16 in Section 4.2). Samples for both $P_2[\vec{A}|\mathcal{M}]$ and $P_3[\vec{A}|\mathcal{M}]$ are colored according to their posterior probability.

parametric model and explain the overstated uncertainty. In Section 4.3, the systematic error is modeled using a Gaussian on \vec{A} as shown in (19), without considering the actual shape of the cross section model $f(\epsilon; \vec{A})$. The resulting posterior cannot exactly capture the correlation which inherently exists between parameters given the cross section model and the datasets. For the $1s_3$ excitation, due to the model definition (4), the two parameters $\{b, \gamma\}$ should be nonlinearly correlated roughly along $\gamma \sim \log b$. Figure 12 shows the individual posteriors in Figure 9 using a log scale for b , which exhibits a clear correlation of $\gamma \sim \log b$. $P_2[\vec{A}|\mathcal{M}]$ (21), which is a joint Gaussian over (b, γ) -space, now looks completely distorted in Figure 12 (a). A significant portion of the distribution deviates from the parameter values that are inferred from the datasets, which contributes to the biased and overstated uncertainty observed earlier.

Of course, in this case, it may be possible to improve the uncertainty model (19) by assuming it to be a joint Gaussian distribution over $(\log b, \gamma)$ -space, instead of (b, γ) . However, such an improvement is predicated upon prior knowledge of the cross section model and the appropriate resulting correlation between the model parameters. Such prior information is often unavailable, particularly for more complex or higher-dimensional models where the implicit dependencies among the parameters are more difficult to understand and characterize.

On the other hand, the Gaussian-process model considers the systematic error on the measurement space (ϵ, σ) directly. As a result, both the goodness-of-fit and the systematic error are evaluated together via (34), against the actual measurement data

\mathcal{M}_m . The resulting posterior properly captures the intrinsic correlation between b and γ arising from the model, without explicitly requiring prior information be built into the model form.

This comparison leads to a conclusion that, among three different perspectives, the probabilistic description in Section 4.4 with a Gaussian-process systematic error most properly reflects the nature of the measurement data. All the cross section uncertainties are thus calibrated with the posterior formulation (28) in Section 4.4. Figure 13 shows the marginal cross section posteriors for all 6 collision processes. For all cross sections, the scattering among the datasets is captured within the credibility intervals. There are some data that lie outside the credibility intervals: in Figure 13 (a), except some outliers between 95–99.7% interval, the elastic cross section samples lie closely around the median value and do not capture the small variation in $\epsilon > 10\text{eV}$; and all the excitation cross sections in Figure 13 (c–f) do not capture the BSR data in $\epsilon - \epsilon_0 < 0.1\text{eV}$. These are, of course, expected results from the cross section models chosen for this uncertainty quantification because the models chosen in Section 3 cannot represent these features. Their parametric uncertainties, therefore, do not reflect any deviation which the models cannot capture, rather ascribing it to the systematic error (including the model inadequacy). However, the resulting parametric uncertainty is still able to encompass the uncertainty in the plasma chemistry and transport properties, which will be shown subsequently.

5.2. Validation with swarm-parameter experiments

The calibrated parametric model for the 6 collision cross sections are forward-propagated to the swarm parameters via BOLSIG+ and compared with the experimental data from Table 3. For the forward propagation, the swarm parameters are evaluated with 7200 samples from the posterior distributions of the model parameters. For each sample, the collision cross section models from Section 3 are evaluated and then used as inputs in BOLSIG+ simulations. BOLSIG+ simulations are run at both the default condition of 300K [6], and also at different background temperatures to match with the experiment conditions in Table 3.

Figure 14 and 15 show the propagated uncertainty in the swarm parameters, compared with the experimental data from Figure 2 and 3. As for the swarm-analysis data in Figure 3, the evaluation of the reduced excitation coefficients in Figure 15 requires the direct excitation cross sections to higher levels, which uncertainties are not considered in the scope of our study. Instead, the nominal cross sections for $2p$ -level excitations are chosen from BSR dataset [18] and included in each sample set of cross sections.

Most of the experimental data lie within 95% credibility intervals of the cross section uncertainty. As mentioned in Section 2.2, in Figure 14 (d) the data from Specht *et al.* [88] deviates from the credibility intervals, as their measurements include contributions from the metastable population. For the transport properties and the reduced ionization

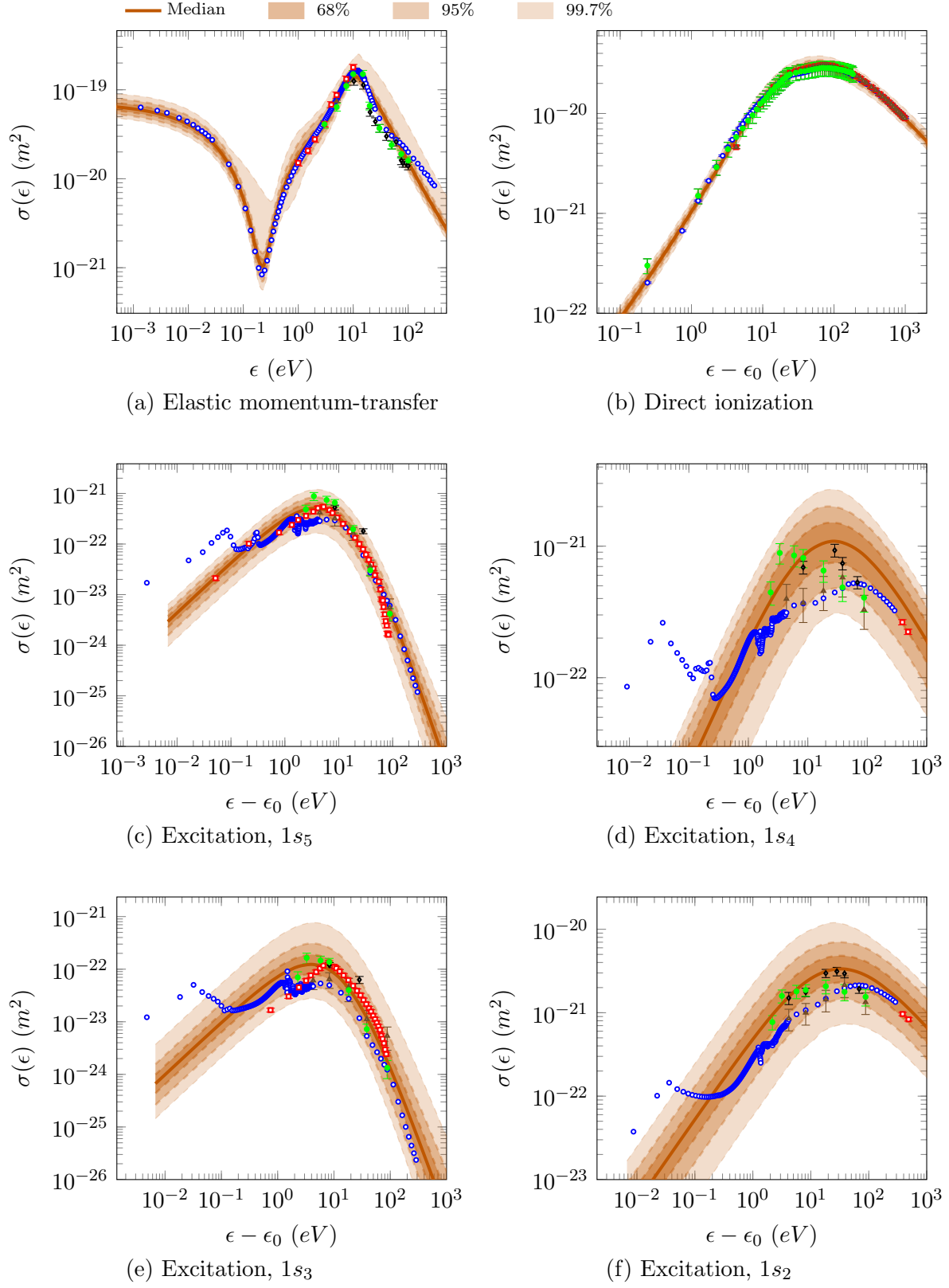


Figure 13. Marginal cross section uncertainty of 6 electron-impact argon collision cross sections, with the Gaussian process representation (Eq. 28 in Section 4.4). Shaded areas indicate the 68%, 95% and 99.7% credibility intervals of the posterior distribution. The measurement data are marked the same as in Figure 1.

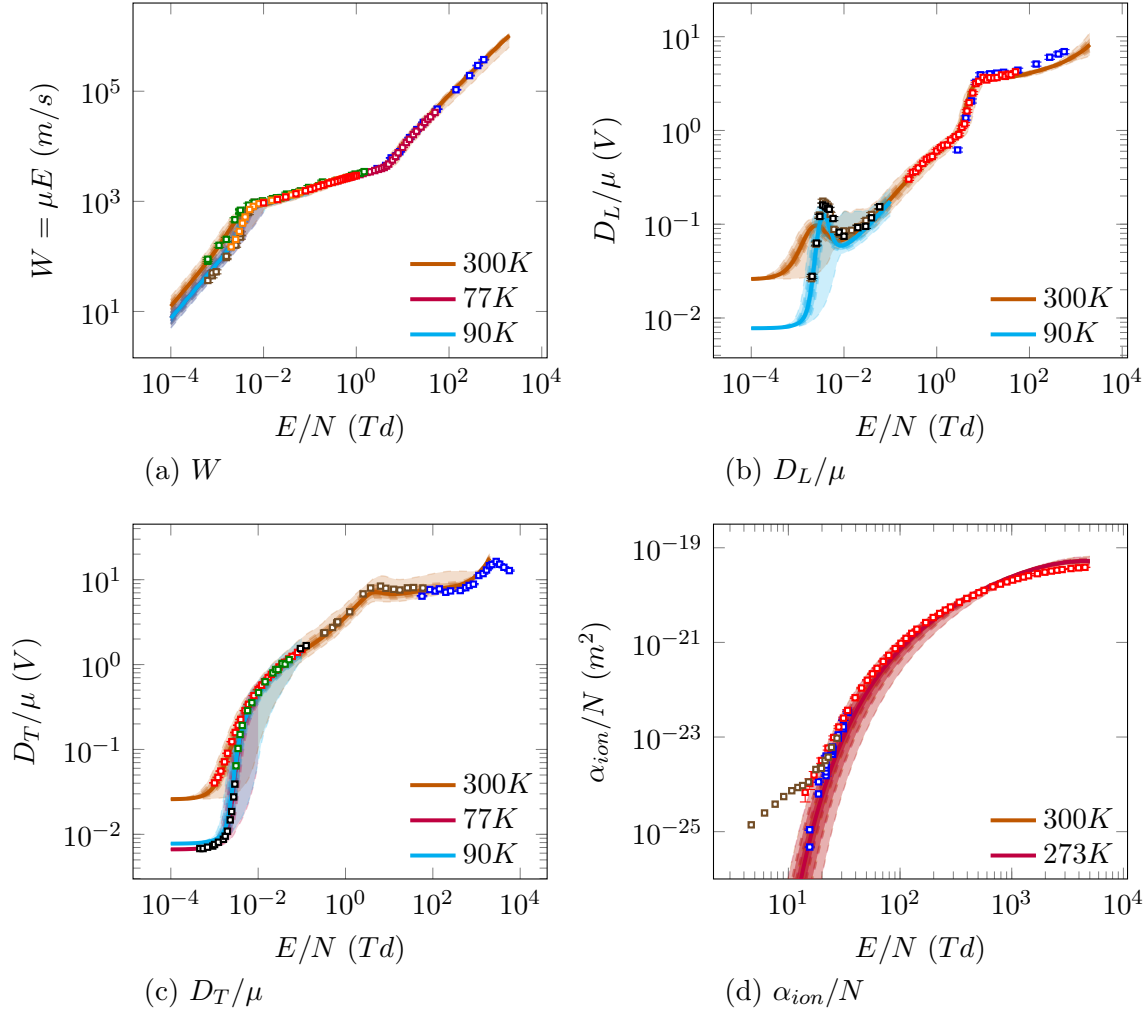


Figure 14. The cross section uncertainty propagated unto the swarm parameters, shown with 3 credibility intervals (68%, 95%, and 99.7%): (a) drift velocity, (b) the ratio of longitudinal diffusivity to mobility, (c) the ratio of transverse diffusivity to mobility, and (d) the reduced ionization coefficient. The measurement data are marked the same as in Figure 2.

coefficients in Figure 14, the impact of the cross section uncertainties was relatively small, and the experimental data also did not exhibit a large discrepancy with each other. On the other hand, the cross section uncertainties have a more significant impact on the reduced excitation coefficients, as shown Figure 15.

6. Conclusion

Cross section uncertainties of 6 e -Ar collision processes are quantified via Bayesian inference. Each cross section is characterized with a semi-empirical model that captures essential features for plasma reaction and transport, so its uncertainty is effectively approximated within a low-dimensional parameter space. Measurement data for cross section inference are curated either from experiments or *ab initio* calculations, into two

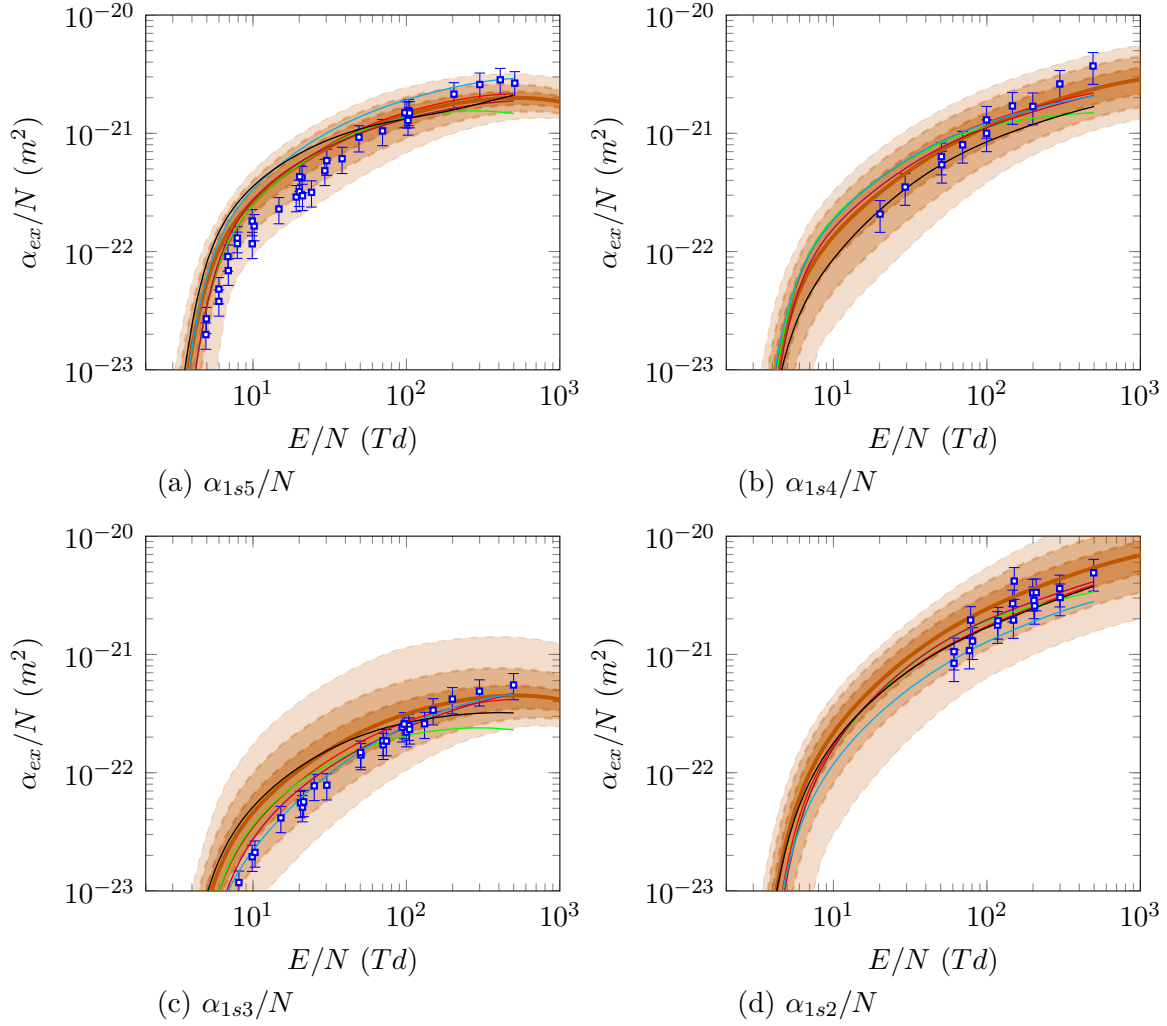


Figure 15. The cross section uncertainty propagated unto the swarm parameters, shown with 3 credibility intervals (68%, 95%, and 99.7%): the reduced excitation coefficients to (a) $1s_5$, (b) $1s_4$, (c) $1s_3$, and (d) $1s_2$. The measurement data are marked the same as in Figure 3.

categories: direct cross section measurement and swarm-parameter measurement. The cross section model parameters are then inferred from the direct cross section data. The resulting distributions are forward-propagated using the **BOLSIG+ 0D** Boltzmann equation solver and validated against the swarm-parameter measurements.

A key aspect of this process is the modeling of discrepancies between different input datasets. Observation errors reported in direct cross section data are often notional, not quantitatively reflecting all systematic errors underlying the experiments. As a result, the discrepancy among datasets is much larger than the reported observation error each claims. No detailed knowledge of these errors, upon which to base a model, is available. Instead, both a parametric representation and a Gaussian-process-based model were developed, with the Gaussian-process-based approach giving better results in the present cases.

The resulting cross section uncertainties quantified by this process provide rich information for the plasma simulations where these calibrated cross sections are used. For example, the impact of each collision process on the macroscopic plasma observables can be evaluated via sensitivity analysis. Furthermore, the uncertainties of collision processes can be forward-propagated through the plasma simulations, thereby evaluating the credibility of the predictive simulations.

As mentioned in Section 2.2, the proposed Bayesian inference framework can be extended to incorporate the swarm-analysis data. As the swarm parameters are determined by the entire set of collisions, including them into the Bayesian inference will provide richer information as to the correlations between the collision processes. Since the measurements are made for the swarm-parameters, evaluating the posterior will require an additional layer of solving the Boltzmann equation model, other than the cross section models themselves. A similar challenge of handling systematic errors/model-form inadequacy is expected, particularly for the excitation rate coefficient data. For example, there are some expected model-form errors which may contribute to the scattering of the data in Figure 15. One might be the approximation for radiative de-excitation processes based on the radiative transition probabilities. The inherent approximation of BOLSIG+ that do not track heavy-species population may also have some contribution to this model-form error.

Acknowledgements

This material is based upon work supported by the Department of Energy, National Nuclear Security Administration under Award Number DE-NA0003969. This work was performed in part under the auspices of the U.S. Department of Energy by Lawrence Livermore National Laboratory under contract DE-AC52-07NA27344. LLNL release number: LLNL-JRNL-851195.

Appendix A. Sensitivity study with BOLSIG+

Appendix A.1. Sensitivity to the elastic collision in the large-energy range

In Section 3.1, the proposed cross section model approximates the high-energy ($> 10\text{eV}$) range with only $\mathcal{O}(\epsilon^{-1})$ asymptote, neglecting smaller-scale variations observed in the measurement datasets.

The impact of this small-scale variations on the plasma transport properties is investigated via BOLSIG+ [16]. The Biagi dataset from the LXCat community [17] is chosen for the baseline cross section set, where $\epsilon > 10\text{eV}$ range of the elastic momentum-transfer cross section is replaced with that from other LXCat datasets [18–21, 67, 71]. Figure A1 (a) shows these manipulated cross section sets, whose $\epsilon > 10\text{eV}$ ranges are scattered similar to the measurement datasets in Figure 5. Figure A1 (b-d) show the plasma transport properties computed at the default BOLSIG+ condition with $300K$. Only slight variations up to 10% are observed in the limited range over $E/N > 300Td$.

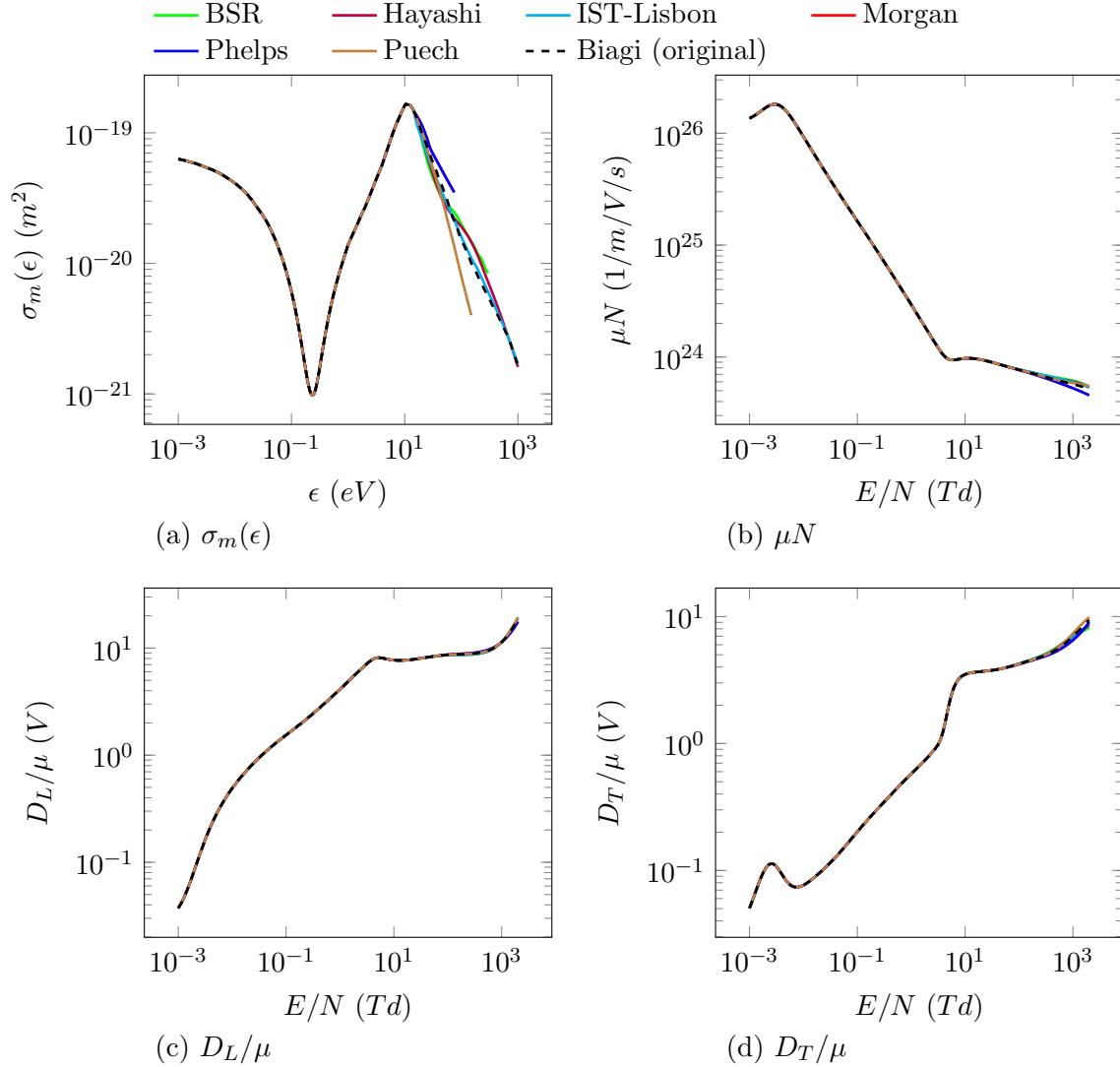


Figure A1. Sensitivity of plasma transport properties to the $\epsilon > 10\text{eV}$ range of the elastic collision: (a) the manipulated elastic cross sections for the analysis, (b) the reduced mobility, (c) the ratio of the longitudinal diffusivity to the mobility, and (d) the ratio of the transverse diffusivity to the mobility computed with corresponding cross section sets.

Appendix A.2. Sensitivity to the small-scale features in the excitation collision

The sensitivity to the small-scale features in the excitation collision is similarly investigated. First, the low energy $\epsilon - \epsilon_0 < 0.3\text{eV}$ range of the baseline Biagi dataset is replaced with that from other datasets [18–21, 67, 71]. In Figure A2 (a), their variations shown are seemingly very large, up to two orders of magnitude. However, in Figure A2 (b), the resulting reaction rate constants surprisingly do not vary from each other.

$\epsilon - \epsilon_0 \in [0.5, 3]\text{eV}$ range of the $1s4$ excitation cross section also exhibits some fine-scale features, which sensitivity is worth investigating. Figure A2 (c) shows the cross

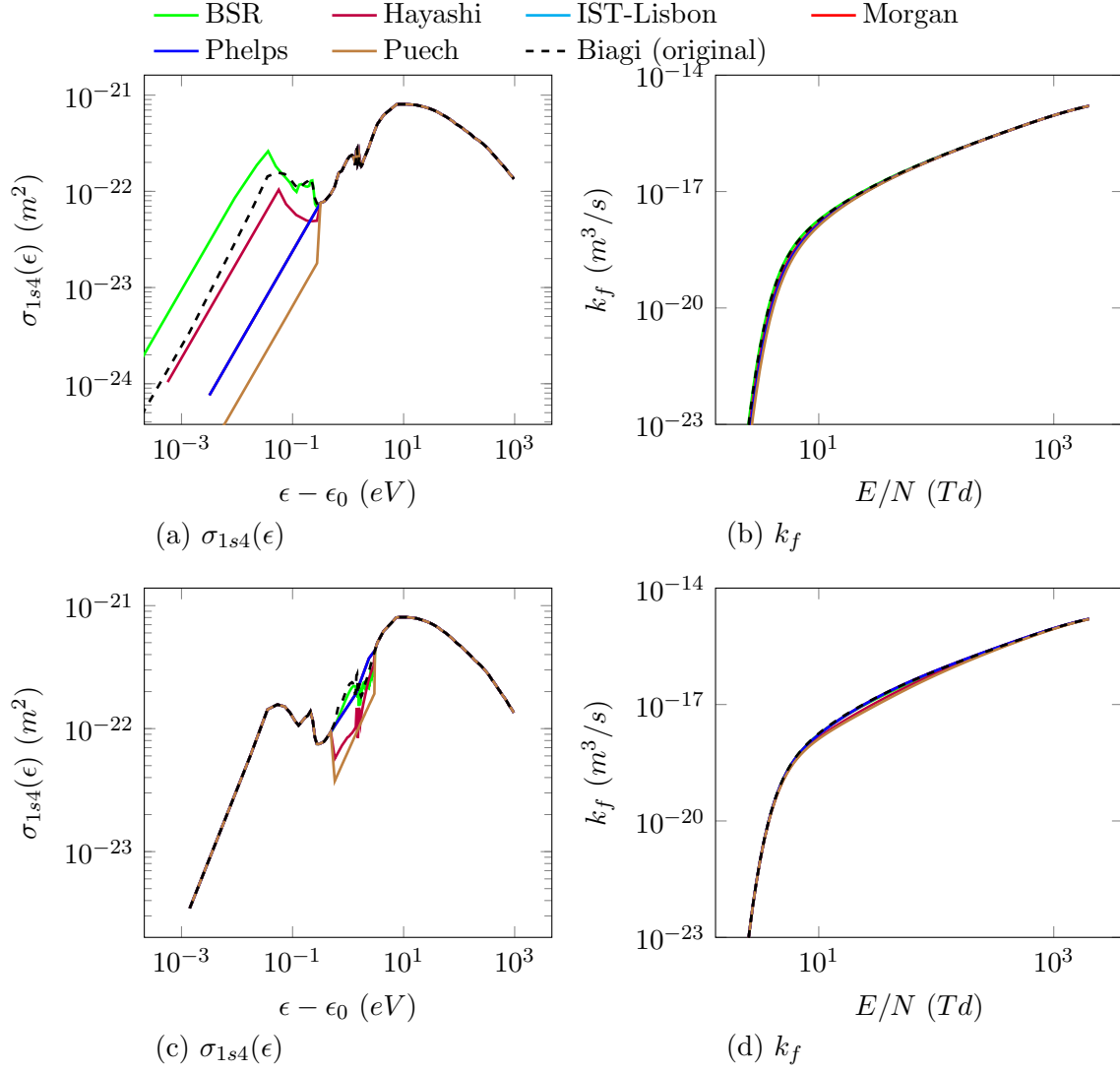


Figure A2. Sensitivity of the reaction rate constant to the small-scale features of the 1s4 excitation collision: (a) the 1s4 excitation cross sections with $\epsilon - \epsilon_0 < 0.3eV$ range manipulated for the analysis, and (b) the corresponding reaction rate constants; (c) the 1s4 excitation cross sections with $\epsilon - \epsilon_0 \in [0.5, 3]eV$ range manipulated for the analysis, and (d) the corresponding reaction rate constants;

sections with this energy range manipulated. While fine-scale features are observed in Biagi, BSR and Hayashi datasets, Phelps and Puech datasets vary smoothly in this energy range. Figure A2 (d) shows the corresponding reaction rate constants, which vary only slightly in the $E/N \in [10, 300]Td$ range. While Hayashi and Puech datasets seem to have lower rate constants, this is rather due to the lower magnitude of their cross sections. They in fact have the rate constants similar to each other, despite their difference of the fine-scale behavior. Likewise, although Phelps dataset completely neglects fine-scale behavior and vary smoothly, it exhibits similar rate constants with Biagi, BSR datasets, due to its similar cross section magnitude. This sensitivity analysis suggests that the plasma reaction rate constants are insensitive to the fine-scale features

in the excitation cross sections.

Similar insensitivity to the low-energy, fine-scale features is observed from other excitation cross sections as well.

References

- [1] Gargioni E and Grosswendt B 2008 *Reviews of Modern Physics* **80** 451–480
- [2] Ferziger J H, Kaper H G and Gross E P 1973 *American Journal of Physics* **41**(4) 601–603 ISSN 0002-9505
- [3] Vlček J 1989 *Journal of Physics D: Applied Physics* **22** 632–643 ISSN 13616463
- [4] Bultel A, van Ootegem B, Bourdon A and Vervisch P 2002 *Physical Review E - Statistical Physics, Plasmas, Fluids, and Related Interdisciplinary Topics* **65** 16 ISSN 1063651X
- [5] Kapper M G and Cambier J L 2011 *Journal of Applied Physics* **109** ISSN 00218979
- [6] Pitchford L, Alves L, Bartschat K, Biagi S, Bordage M, Phelps A, Ferreira C, Hagelaar G, Morgan W, Pancheshnyi S *et al.* 2013 *Journal of Physics D: Applied Physics* **46** 334001
- [7] Pitchford L C, Alves L L, Bartschat K, Biagi S F, Bordage M C, Bray I, Brion C E, Brunger M J, Campbell L, Chachereau A *et al.* 2017 *Plasma Processes and Polymers* **14** 1600098
- [8] Oran E, Oh C and Cybyk B 1998 *Annual Review of Fluid Mechanics* **30** 403–441
- [9] Bird G A 1994 *Molecular gas dynamics and the direct simulation of gas flows*
- [10] Birdsall C K 1991 *IEEE Transactions on plasma science* **19** 65–85
- [11] Vahedi V, DiPeso G, Birdsall C, Lieberman M and Rognlien T 1993 *Plasma Sources Science and Technology* **2** 261
- [12] Birdsall C K and Langdon A B 2004 *Plasma physics via computer simulation* (CRC press)
- [13] Vassiliev O N, Wareing T A, McGhee J, Failla G, Salehpour M R and Mourtada F 2010 *Physics in Medicine & Biology* **55** 581
- [14] St Aubin J, Keyvanloo A, Vassiliev O and Fallone B 2015 *Medical physics* **42** 780–793
- [15] Vassiliev O N 2017 *Grid Based Boltzmann Equation Solvers* (Cham: Springer International Publishing) pp 225–250 ISBN 978-3-319-44141-2 URL https://doi.org/10.1007/978-3-319-44141-2_7
- [16] Hagelaar G J and Pitchford L C 2005 *Plasma Sources Science and Technology* **14** 722–733 ISSN 09630252
- [17] Biagi database retrieved on October 14, 2021 URL <https://www.lxcat.net>
- [18] BSR database retrieved on October 14, 2021 URL <https://www.lxcat.net>
- [19] Hayashi database retrieved on October 14, 2021 URL <https://www.lxcat.net>

- [20] IST-Lisbon database retrieved on October 14, 2021 URL <https://www.lxcat.net>
- [21] Puech database retrieved on October 14, 2021 URL <https://www.lxcat.net>
- [22] Stuart A M 2010 *Acta numerica* **19** 451–559 ISSN 0962-4929
- [23] Smith R C 2013 *Uncertainty quantification: theory, implementation, and applications* vol 12 (Siam)
- [24] Kennedy M C and O’Hagan A 2001 *Journal of the Royal Statistical Society. Series B: Statistical Methodology* **63** 425–464
- [25] Rasmussen C E and Williams C K I 2006 *Gaussian Processes for Machine Learning* vol 7 (MIT Press) ISBN 026218253X
- [26] Foreman-Mackey D, Hogg D W, Lang D and Goodman J 2013 *Publications of the Astronomical Society of the Pacific* **125** 306–312 (*Preprint* 1202.3665)
- [27] Bederson B and Kieffer L 1971 *Reviews of Modern Physics* **43** 601
- [28] A R Filippelli C C L and Anderson L W 1994 *Advances in Atomic, Molecular, and Optical Physics* **33** URL <https://www.osti.gov/biblio/241114>
- [29] Tachibana K 1986 *Physical Review A* **34** 1007
- [30] Chilton J E, Boffard J B, Schappe R S and Lin C C 1998 *Physical Review A* **57** 267
- [31] Milloy H B, Crompton R W, Rees J A and Robertson A G 1977 *Australian Journal of Physics* **30** 61–72
- [32] Haddad G and O’Malley T 1982 *Australian Journal of Physics* **35** 35–40
- [33] Nakamura Y 1987 *Journal of Physics D: Applied Physics* **20** 933–938 URL <https://doi.org/10.1088/0022-3727/20/7/016>
- [34] Biagi S F 1989 *Nuclear Instruments and Methods in Physics Research Section A: Accelerators, Spectrometers, Detectors and Associated Equipment* **283** 716–722
- [35] Yanguas-Gil A, Cotrino J and Alves L 2005 *Journal of Physics D Applied Physics* **38** 1588–1598
- [36] Zatsarinny O and Bartschat K 2013 *Journal of Physics B: Atomic, Molecular and Optical Physics* **46** 112001
- [37] McEachran R and Stauffer A 2014 *The European Physical Journal D* **68** 1–8
- [38] Gangwar R, Sharma L, Srivastava R and Stauffer A 2012 *Journal of Applied Physics* **111** 053307
- [39] Zatsarinny O and Bartschat K 2004 *Journal of Physics B: Atomic, Molecular and Optical Physics* **37** 4693
- [40] Zatsarinny O, Wang Y and Bartschat K 2014 *Phys. Rev. A* **89**(2) 022706 URL <https://link.aps.org/doi/10.1103/PhysRevA.89.022706>
- [41] Allan M, Zatsarinny O and Bartschat K 2006 *Physical Review A* **74** 030701
- [42] Khakoo M A, Zatsarinny O and Bartschat K 2011 *Journal of Physics B: Atomic, Molecular and Optical Physics* **44** 015201 URL <https://doi.org/10.1088/0953-4075/44/1/015201>

- [43] Bretagne J, Calde G, Legentil M and Puech V 1986 *Journal of Physics D: Applied Physics* **19** 761
- [44] Kim Y K and Rudd M E 1994 *Physical Review A* **50** 3954–3967
- [45] Srivastava S, Tanaka H, Chutjian A and Trajmar S 1981 *Physical Review A* **23** 2156
- [46] Gibson J C, Gulley R, Sullivan J, Buckman S, Chan V and Burrow P 1996 *Journal of Physics B: Atomic, Molecular and Optical Physics* **29** 3177
- [47] Panajotovic R, Filipovic D, Marinkovic B, Pejcev V, Kurepa M and Vuskovic L 1997 *Journal of Physics B: Atomic, Molecular and Optical Physics* **30** 5877
- [48] Mielewska B, Linert I, King G C and Zubek M 2004 *Physical Review A* **69** 062716
- [49] Rapp D and Englander-Golden P 1965 *The Journal of Chemical Physics* **43** 1464–1479 (Preprint <https://doi.org/10.1063/1.1696957>) URL <https://doi.org/10.1063/1.1696957>
- [50] Wetzel R C, Baiocchi F A, Hayes T R and Freund R S 1987 *Physical Review A* **35** 559–577 ISSN 10502947
- [51] Straub H, Renault P, Lindsay B, Smith K and Stebbings R 1995 *Physical Review A* **52** 1115
- [52] Chutjian A and Cartwright D 1981 *Physical Review A* **23** 2178
- [53] Li G P, Takayanagi T, Wakiya K, Suzuki H, Ajiro T, Yagi S, Kano S S and Takuma H 1988 *Physical Review A* **38** 1240–1247 ISSN 10502947
- [54] Schappe R S, Schulman M B, Anderson L W and Lin C C 1994 *Physical Review A* **50** 444–461 ISSN 10502947
- [55] Filipovic D M, Marinkovic B P, Pejcev V and Vuskovic L 2000 *Journal of Physics B: Atomic and Molecular and Optical Physics* **33** 677
- [56] Filipovic D, Marinkovic B, Pejcev V and Vuskovic L 2000 *Journal of Physics B: Atomic, Molecular and Optical Physics* **33** 2081
- [57] Khakoo M A, Vandeventer P, Childers J G, Kanik I, Fontes C J, Bartschat K, Zeman V, Madison D H, Saxena S, Srivastava R and Stauffer A D 2004 *Journal of Physics B: Atomic, Molecular and Optical Physics* **37** 247–281 ISSN 09534075
- [58] Buckman S, Hammond P, King G and Read F 1983 *Journal of Physics B: Atomic and Molecular Physics (1968-1987)* **16** 4219
- [59] Biagi S F 1988 *Nuclear Instruments and Methods in Physics Research Section A: Accelerators, Spectrometers, Detectors and Associated Equipment* **273** 533–535
- [60] Hayashi M 2003 *Institute for Fusion Science*
- [61] Alves L L 2014 *Journal of Physics: Conference Series* **565** 012007 URL <https://doi.org/10.1088/1742-6596/565/1/012007>
- [62] Yamabe C, Buckman S J and Phelps A V 1983 *Phys. Rev. A* **27**(3) 1345–1352 URL <https://link.aps.org/doi/10.1103/PhysRevA.27.1345>

- [63] Weber T, Boffard J B and Lin C C 2003 *Physical Review A* **68** 032719
- [64] Drawin H W 1967 *Fontenay-aux-Roses* URL <https://www.osti.gov/biblio/4675184>
- [65] Lee C M and Lu K 1973 *Physical Review A* **8** 1241
- [66] Bretagne J, Godart J and Puech V 1982 *Journal of Physics D: Applied Physics* **15** 2205
- [67] Morgan database retrieved on October 14, 2021 URL <https://www.lxcat.net>
- [68] Puech V and Torchin L 1986 *Journal of Physics D: Applied Physics* **19** 2309–2323 URL <https://doi.org/10.1088/0022-3727/19/12/011>
- [69] Frost L S and Phelps A V 1964 *Phys. Rev.* **136**(6A) A1538–A1545 URL <https://link.aps.org/doi/10.1103/PhysRev.136.A1538>
- [70] Tachibana K and Phelps A V 1981 *The Journal of Chemical Physics* **75** 3315–3320 (*Preprint* <https://doi.org/10.1063/1.442483>) URL <https://doi.org/10.1063/1.442483>
- [71] Phelps database retrieved on October 14, 2021 URL <https://www.lxcat.net>
- [72] Fletcher J and Burch D 1972 *Journal of Physics D: Applied Physics* **5** 2037
- [73] Schaper M and Scheibner H 1969 *Beiträge aus der Plasmaphysik* **9** 45–57
- [74] Smith P T 1930 *Phys. Rev.* **36**(8) 1293–1302 URL <https://link.aps.org/doi/10.1103/PhysRev.36.1293>
- [75] Nakamura Y and Kurachi M 1988 *Journal of Physics D: Applied Physics* **21** 718–723 URL <https://doi.org/10.1088/0022-3727/21/5/008>
- [76] Fon W, Berrington K, Burke P and Hibbert A 1983 *Journal of Physics B: Atomic and Molecular Physics* **16** 307
- [77] Ferreira C and Loureiro J 1983 *Journal of Physics D: Applied Physics* **16** 2471
- [78] Townsend J and Bailey V 1922 *The London, Edinburgh, and Dublin Philosophical Magazine and Journal of Science* **44** 1033–1052
- [79] Pack J and Phelps A 1961 *Physical Review* **121** 798
- [80] Warren R W and Parker Jr J H 1962 *Physical Review* **128** 2661
- [81] Robertson A and Rees J 1972 *Australian Journal of Physics* **25** 637–640
- [82] Robertson A 1977 *Australian Journal of Physics* **30** 39–50
- [83] Milloy H and Crompton R 1977 *Australian Journal of Physics* **30** 51–60
- [84] Kucukarpaci H and Lucas J 1981 *Journal of Physics D: Applied Physics* **14** 2001
- [85] Al-Amin S A and Lucas J 1987 *Journal of Physics D: Applied Physics* **20** 1590–1595 ISSN 00223727
- [86] Golden D E and Fisher L H 1961 *Physical Review* **123** 1079–1086 ISSN 0031899X
- [87] Kruithof A 1940 *Physica* **7** 519–540
- [88] Specht L, Lawton S and DeTemple T 1980 *Journal of Applied Physics* **51** 166–170

- [89] Wiese W L, Smith M W and Miles B 1969 Atomic transition probabilities. volume 2. sodium through calcium Tech. rep. NATIONAL STANDARD REFERENCE DATA SYSTEM
- [90] Crompton R 1994 *Advances in atomic, molecular, and optical physics* **33**
- [91] O'Malley T F 1963 *Physical Review* **130** 1020–1029 ISSN 0031899X
- [92] Kramida A, Yu Ralchenko, Reader J and NIST ASD Team 2022 NIST Atomic Spectra Database (ver. 5.10), [Online]. Available: <https://physics.nist.gov/asd> [2022, November 7]. National Institute of Standards and Technology, Gaithersburg, MD.